Direct Numerical Simulation of Turbulent Heat Transfer at Low Prandtl Numbers in Planar Impinging Jets

M. Duponcheel, Y. Bartosiewicz

Université catholique de Louvain (UCLouvain), Institute of Mechanics, Materials and Civil Engineering (iMMC), B-1348, Louvain-la-Neuve, Belgium

Abstract

DNS simulations of planar impinging jets are performed to provide reference data to validate RANS models for low-Prandtl turbulent heat transfer. In that configuration, a hot plane jet is blown from a slot at the top wall of a channel and impinges on the cooler bottom wall. The present DNS simulations are carried out at $Re = 4000$ and 5700, based on the jet width and velocity, and for Pr down to 0.01. Two cases are investigated: the case of a laminar uniform jet profile and the case of a fully turbulent inlet profile coming from an auxiliary channel flow simulation running in parallel. The DNS results show how the heat transfer in this configuration evolves from the turbulence-dominated case at $Pr = 1$ to the molecular diffusion-dominate case at $Pr = 0.01$. The temperature field at $Pr = 0.01$ is much smoother than at higher Prandtl number because the much larger heat diffusivity quickly diffuses the temperature fluctuations. The comparison between the laminar and the fully-developed turbulent inflows also show different heat transfer characteristics in the vicinity of the stagnation point, depending on the presence of velocity fluctuations in the bottom-wall boundary layers.

Keywords:
DNS, Heat Transfer, low Prandtl number, Planar Impinging Jet

1. Introduction

Liquid metals such as Sodium or Lead-Bismuth Eutectic (LBE) are envisioned as coolant in several GenIV fast reactor concepts, e.g ASTRID [1] or MYRRHA [2]. Regarding heat transfer, one of the main characteristics of liquid metals is their low Prandtl numbers, $Pr = \nu/\alpha$ with ν the kinematic viscosity and the heat diffusivity. Consequently, the Reynolds analogy, typically used to compute turbulent heat transfer, is known to fail for such fluids (Grötzbach [3]) and a proper validation of the computational tools used in the design of those systems is therefore required, also for advanced RANS (Reynolds Averaged Navier-Stokes) models including 4-equation models (Manservisi and Menghini [4]) and non-linear Algebraic Heat Flux Models (Shams et al. [5]). Such a validation effort relies heavily on experimental data but Direct Numerical Simulation (DNS) data are also very useful to derive, calibrate and validate engineering RANS models.

During the EC-funded THINS project [6], new DNS reference data for low Pr heat transfer were obtained in forced convection for fully-developed confined turbulent flows, such as channel flows (Duponcheel et al. [7] and Tiselj [8]) or wavy channel flows (Errico and Stalio [9]). But further validation cases are definitely required for other flow conditions, such as mixed convection, and in other configurations, such as unbounded flows or in more complex wall-bounded flows, including boundary layer separation. The present work deals with heat transfer in non-developed wall-bounded flows by studying impinging plane jets where a hot jet is blown from a slit in the top wall of a channel and impinges on the cooler bottom wall.

Impinging jets have been widely investigated both experimentally and numerically for $Pr \approx 1$, as reviewed by Carlomagno and Ianiro [10], because they are of both fundamental and of practical interest: on the one hand, this constitute a canonical case of interaction between a developing turbulent flow and a wall, on the other hand, they constitute an efficient way of cooling a surface and are therefore used in various applications such as gas turbine blade cooling [11], and many others.

Different configurations of impinging jets can be encountered, mostly depending on the shape of the jet (round or planar), the ratio between the jet width/diameter and the distance between the nozzle and the impinged wall, the initial jet profile, etc. The case of the round jet has been the most studied by many authors, e.g. see Nishino et al. [12], Satake and Kunugi [13], Hadziabdic and Hanjalic [14], Violato et al. [15], Dairay et al. [16]. More recently, He and Liu [17] investigated by LES the heat transfer enhancement of an impinging jet issued from a lobed nozzle at two aspect ratio, while Taghinia and Rahman [18] analyzed the influence of the subgrid scale modeling also for the case of the round jet. The plane jet was studied experimentally by Sakakibara et al. [19] and Sakakibara et al. [20] who studied the vortical structures in the jet and near the stagnation region. They showed that counter-rotating vortex pairs are responsible for turbulent mixing in the stagnation region. These vortex pairs find their origin in vortical structures forming in the jet. Hattori and Nagano [21] performed DNS simulations of impinging planar jets at moderate Reynolds number and for various aspect ratio, i.e. the ratio between the jet width and the wall distance. The used fully developed channel flows as inlet conditions for the jet. They studied the effect of the aspect ratio on the Nusselt Nu number along the impinged wall at $Pr = 0.71$. They showed that, for very small aspect ratio, a secondary maximum can be found in the Nu profile away from the stagnation point, whereas the profile is monotonously decreasing for higher aspect ratios. Jaramillo et al. [22] also used DNS to study a higher Re plane jet with a higher aspect ratio of 4. They used a flat profile for the jet inlet. In that case, they also observed a secondary maximum in the Nu profile. Later, Aillaud et al. [23] used LES to investigate the physics leading to this secondary peak in the Nu in the case of the round jet.

In the present work, DNS are performed for impinging plane jets at moderate Reynolds numbers and for both laminar and turbulent jet inlets. The heat transfer is computed for Prandtl numbers down to 0.01.

This paper is organized as follows. First, the numerical method is described followed by the setup of the simulations. The flow description as well as analysis of results are then presented. Finally, conclusions are drawn.

2. Numerical method

The governing equations are the Navier-Stokes equations for incompressible flows and the energy equation with constant physical properties. These equations are solved using a fractional-step method. The equations are discretized in space using the fourth order finite difference scheme of Vasilyev [24], which is such that the discretized convective term conserves the discrete energy on cartesian stretched meshes. This is an important characteristic for direct numerical simulations of turbulent flows. The Poisson equation for the pressure is solved using an efficient parallel multigrid solver which is either used directly or as a preconditioner for a conjugate gradient solver. The equations are integrated in time using a second order Adams-Bashforth time-stepping. At low Prandtl number, subtime-stepping is used for the temperature equation because of the very small heat conduction time-scale which is more stringent that the convective time-scale, i.e. the CFL condition.

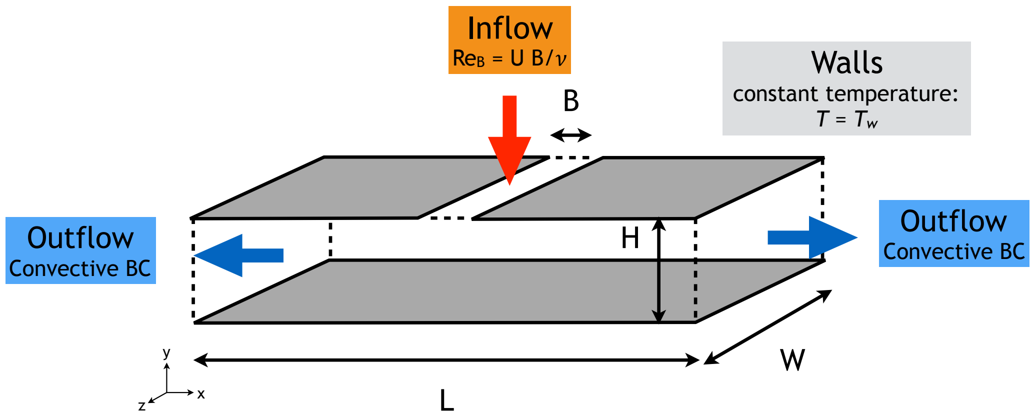

Figure 1: Sketch of the computational setup.

3. Simulation setup

The setup of the plane impinging jet consists of two infinite parallel flat plates where the top plate is split by a slit through which fluid is injected to form the jet, which impinges on the bottom plate. The problem is simulated in a rectangular box where the top ($y = H$) and bottom ($y = 0$) surfaces coincide with the walls and the top surface also contains the slit ($y = H$ and $-B/2 < x < B/2$). In the mean flow direction, far away from the jet, at $x = -L/2$ and $L/2$, convective outflow boundary conditions are used, whereas the flow is considered periodic in the spanwise direction (z), in which the domain length is W. This configuration is sketched in Fig 1.

The top and bottom walls are isothermal, so that $u_i = 0$ and $T = T_w$ when $y = 0$ and when $y = H$ and $|x| \geq B/2$. In the slit ($y = H$ and $|x| < B/2$), the inlet jet profile is imposed. Two cases were considered:

- flat laminar profile : $(u, v, w) = (0, -U, 0)$,
- fully developed turbulent profile : $u_i(x, H, z) = u_{i,channel}(x, y_0, z)$,

but in both cases, the jet is isothermal $T = T_j$. In the turbulent case, this indeed corresponds to the asymptotic solution of the case with isothermal walls at T_j. The temperature difference between the jet and the walls is $\Delta T = T_j - T_w$. The channel flow solution $u_{i,channel}$ is extracted in an arbitrary plane $y = y_0$ of the auxiliary channel flow simulation running simultaneously with the main jet simulation, as explained in Section 5.1. The

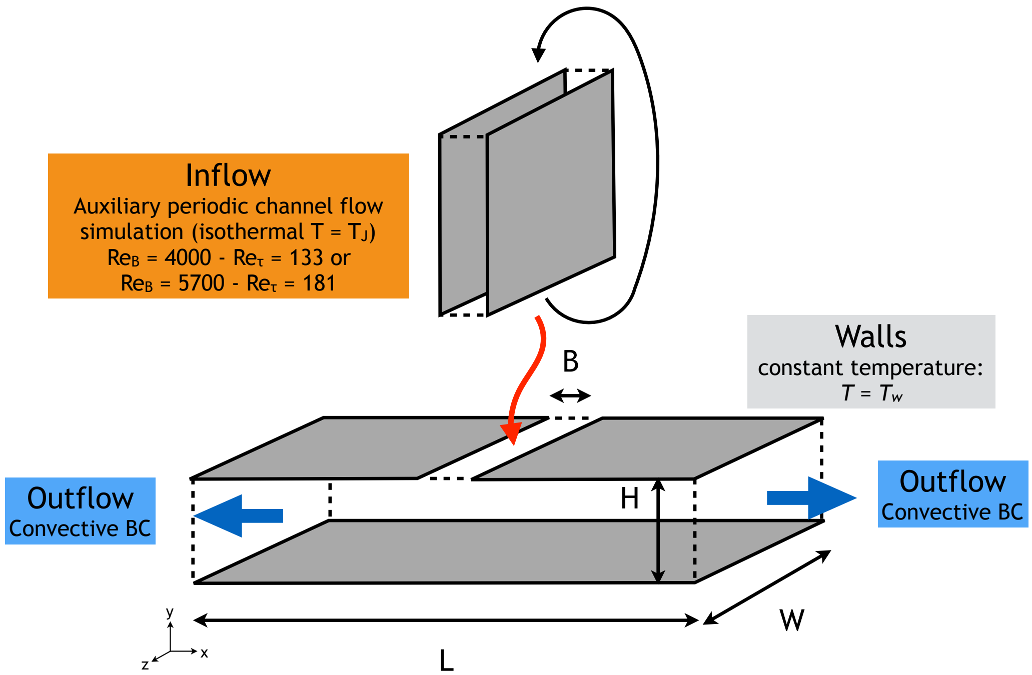

Figure 2: Computational setup for the turbulent inlet case with the auxiliary simulation.

coupled configuration is represented in Fig 2. The flow can be characterized by the Reynolds number based on the jet mean velocity U and the jet width B: $Re = \frac{UB}{\nu}$, with ν, the kinematic viscosity. This Re is also the bulk Reynolds number of the auxiliary channel, which can also be characterized by the friction Reynolds number $Re_\tau = \frac{\bar{u}_\tau(B/2)}{\nu}$, where $\bar{u}_\tau = \sqrt{\bar{\tau}_w/\rho}$ is the friction velocity, with $\bar{\tau}_w$ the mean wall shear stress. The temperature field, characterized by the Prandtl number $Pr = \nu/\alpha$, was simulated for $Pr = 1 - 0.1 - 0.01$ in all cases.

The impinging jet is also characterized by the dimensionless jet-to-surface spacing, also called Aspect Ratio $AR = H/B$. In the previous DNS, Hattori and Nagano [21] considered the case $AR = 2$ whereas Jaramillo et al. [22] used $AR = 4$. A higher aspect ratio may be desirable in order to be closer to a free impinging jet, while low AR cases are more confined. However, high AR cases are very expensive because they also required longer domains: Jaramillo et al. [22] showed that, for $AR = 4$, the domain must be at least $40B$-long on each side of the jet so that the outflow boundaries have a negligible effect on the recirculation region. Furthermore, increasing AR also increases the

Table 1: Simulation parameters

	Re_B	Pr	$L/B \times H/B \times W/B$	$N_x \times N_y \times N_z$	Inlet
Ref. [21]	4560	0.71	$26 \times 2 \times 1.6$	$320 \times 96 \times 96$	fully turbulent
Ref. [22]	20000	0.71	$100 \times 4 \times 2\pi$	$1680 \times 368 \times 168$	flat laminar
present DNS:					
L4000	4000	1.0-0.1-0.01	$80 \times 2 \times \pi$	$2048 \times 144 \times 128$	flat laminar
T4000	4000	1.0-0.1-0.01	$80 \times 2 \times \pi$	$2048 \times 144 \times 128$	fully turbulent
T5700	5700	1.0-0.1-0.01	$80 \times 2 \times \pi$	$2560 \times 192 \times 128$	fully turbulent

physical time required for a perturbation to leave the domain since the mean velocity between the plates, towards the outflow boundaries, is $U/(2\,AR)$. Therefore, a small aspect ratio case is considered here: $AR = 2$, similarly to Hattori and Nagano [21], but with a much longer domain so that the outflow has negligible influence on the jet region: $L/B = 80$, as proposed by Jaramillo et al. [22] for the $AR = 4$ case, which is thus conservative in the present case.

The main characteristics of the mesh are given in Table 2 and the x and y mesh size profiles are drawn in Fig. 3. Those final meshes were obtained after several preliminary simulations to adjust and optimize the local grid sizes. The smallest Δx cells are located in the shear-layer region of the jet. The minimum size was determined using the near-wall resolution of the auxiliary channel flow (see Table 3). The axial mesh size increases very slowly in the region $1 < x < 10$, where most of jet-wall interaction occurs. Then, the mesh size increases significantly up to the outflow. In the wall-normal direction, the mesh is refined close to both walls but preferentially towards the lower wall where the largest wall-fluxes are expected. The domain and resolution of the auxiliary channel flow simulation used to generate the inflow data are given in Table 3 in the conventional channel flow axes, i.e. with x the streamwise direction, whereas the actual jet direction is y. The domain size is the same as that used by Kim et al. [25] at $Re_\tau = 180$ and the resolutions are typical of channel flow DNS simulations [25, 26].

The suitability of the mesh for the DNS of the flow can be assessed a-posteriori. Table 4 gives the maximum near-wall mesh size in wall units as computed using the local shear-stress. The maximum Δx^+ is evaluated for $|x|/B < 20$ because the actual maximum is obtained at the outflow, where Δx is maximum. The latter value is also given as $\Delta x^+_{outflow}$ in Table 4.

Table 2: Grid spacing

Re	$\Delta x_{min}/B$	$\Delta x_{max}/B$	$\Delta y_{min}/B$	$\Delta y_{max}/B$	$\Delta z/B$
20000 [22]	9.23×10^{-4}		5.28×10^{-3}	-	3.74×10^{-2}
4000	4.67×10^{-3}	1.68×10^{-1}	5.00×10^{-3}	1.94×10^{-2}	2.45×10^{-2}
5700	2.75×10^{-3}	1.41×10^{-1}	3.80×10^{-3}	1.52×10^{-2}	2.45×10^{-2}

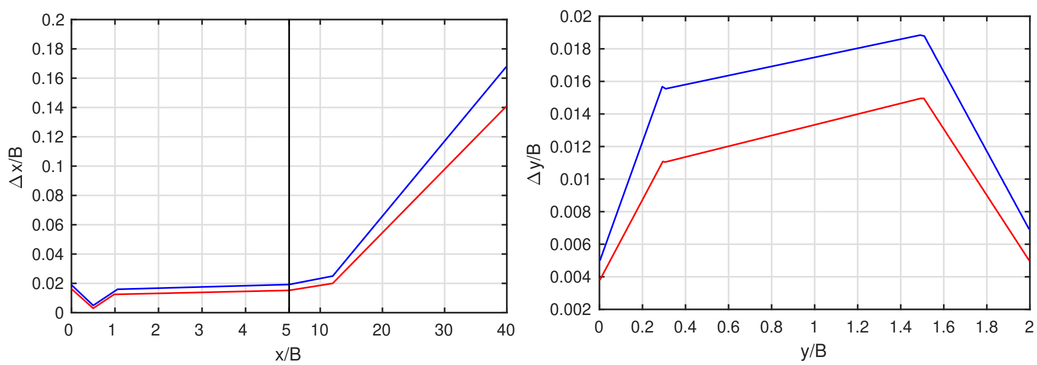

Figure 3: Horizontal x (left) and wall-normal y (right) mesh size profiles : $Re = 4000$ mesh (blue) and $Re = 5700$ mesh (red).

Table 3: Auxiliary channel flow parameters (given in the conventional channel flow axes)

Re_B	Re_τ	$L_x/B \times L_y/B \times L_z/B$	$N_x \times N_y \times N_z$	Δx^+	Δy^+_{min}	Δz^+
4000	133	$2\pi \times 1 \times \pi$	$128 \times 96 \times 128$	13.0	0.62	6.5
5700	181	$2\pi \times 1 \times \pi$	$256 \times 128 \times 128$	8.9	0.50	8.9

Table 4: Near-wall mesh quality

	Δx^+_{max}	$\Delta x^+_{outflow}$	$y^+_{1,max}$	Δz^+_{max}
L4000	6.9	13.7	1.1	10.6
T4000	8.0	13.1	1.3	12.6
T5700	8.3	15.9	1.3	16.4

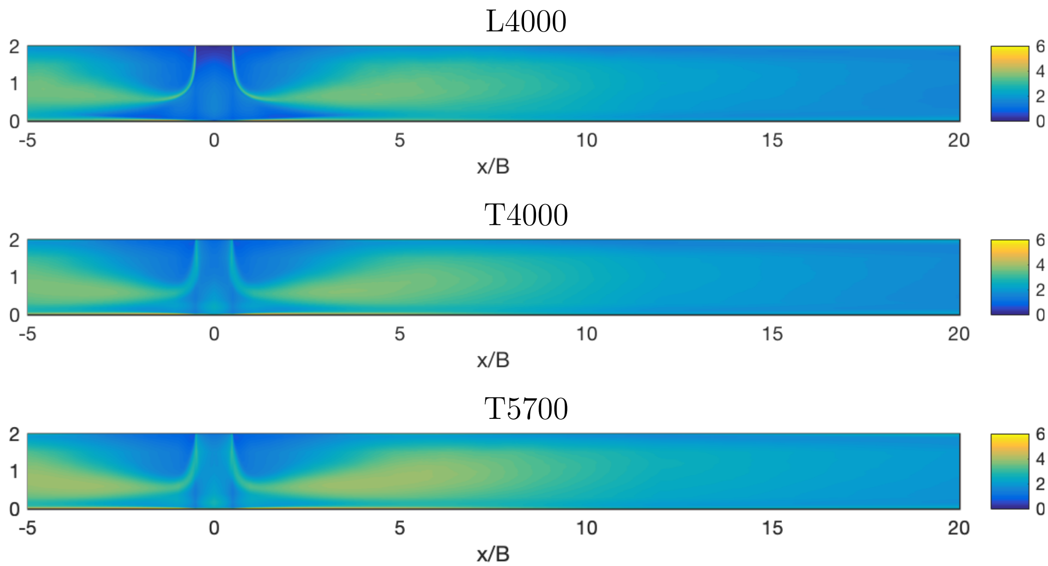

Figure 4: Visualization of the cell-size to Kolmogorow scale ratio Δ/η for the three simulations.

The obtained values are suitable for a DNS of a turbulent wall-bounded flow with $\Delta x^+ < 10$ and $y^+_{1,max} \approx 1$, even though the maximum Δz^+ values are relatively high for DNS. The averaged values are obviously lower than these maximum values. It can also be observed than the Δz cell size of the present simulations is still smaller than that used by Jaramillo et al. [22] at $Re = 20000$. In order to evaluate the mesh quality inside the domain, the ratio of the mesh size $\Delta = (\Delta x\, \Delta y\, \Delta z)^{1/3}$ to the Kolmogorov scale $\eta = (\nu^3/\bar{\epsilon})^{1/4}$ is shown in Fig. 4. The maximum in the bulk of the flow is about $\Delta/\eta \approx 3-4$ whereas very local values of about 5-6 can be obtained very near the jet inlet corner, in the laminar inlet case at $Re = 4000$, or very close to the wall, where the Δ mesh size is increased by the wall-parallel grid spacings. This overall shows that the mesh can be considered appropriate to perform the DNS of the impinging jet flow.

Table 5: Time-stepping parameters

	$\Delta t U/B$	$t_{end} U/B$	$t_{avg} U/B$
L4000	7.5×10^{-4}	251	97
T4000	7.5×10^{-4}	686	521
T5700	5.0×10^{-4}	514	354

The time-step of the simulations are given in Table 5 and are such that $CFL_{max} < 0.15$ in all directions. The characteristic time of the jet is B/U while the dimensionless time required for a perturbation to travel from the jet to one outflow is of the order of $\frac{t_L U}{B} = \frac{2\,AR\,L}{U}\frac{U}{B} = 160$. The simulations were always started from the results of another preliminary or production simulation. The simulations were then run for at least $\frac{t_L U}{2B}$ before statistics were gathered, so that the region of interest near the jet has reached a statistically steady state. The convergence of the statistics can be evaluated by comparing the results of different averaging windows. This is shown in Figs. 5 and 6 for the turbulent inlet cases at $Re = 4000$ and 5700, respectively, with the temperature profiles at the three Pr and with the streamwise and wall-normal velocity fluctuations. This shows that, in both cases, the mean profiles are very well converged since the profiles in all the averaging windows essentially collapse. For the fluctuations, some differences are visible between the smaller averaging windows. The T5700 case was simulated on 1030 cores (1024 for the main simulation and 8 for the auxiliary channel) for 905000 h.CPU.

4. Description of the flow

Instantaneous visualizations of the flow in a vertical (x-y) plane through the domain are presented in Figs. 7, 8 and 9, for the L4000, T4000 and T5700 cases, respectively. The velocity magnitude, the spanwise vorticity ω_z and the temperature fields at the three Prandtl numbers are displayed. In the L4000 case, the uniform inlet profile of the jet can be observed which results in a large potential core. The shear layers at the boundary of the jet only become unstable when the jet is deflected by the presence of the lower wall. Thin boundary layers develop on the lower wall, starting from the stagnation point in the center of the jet. They become turbulent around $x/B = 4$, where the whole deflected jets also transition to turbulence. The effect of the Prandtl number on the different temperature fields is also significant as the gradients

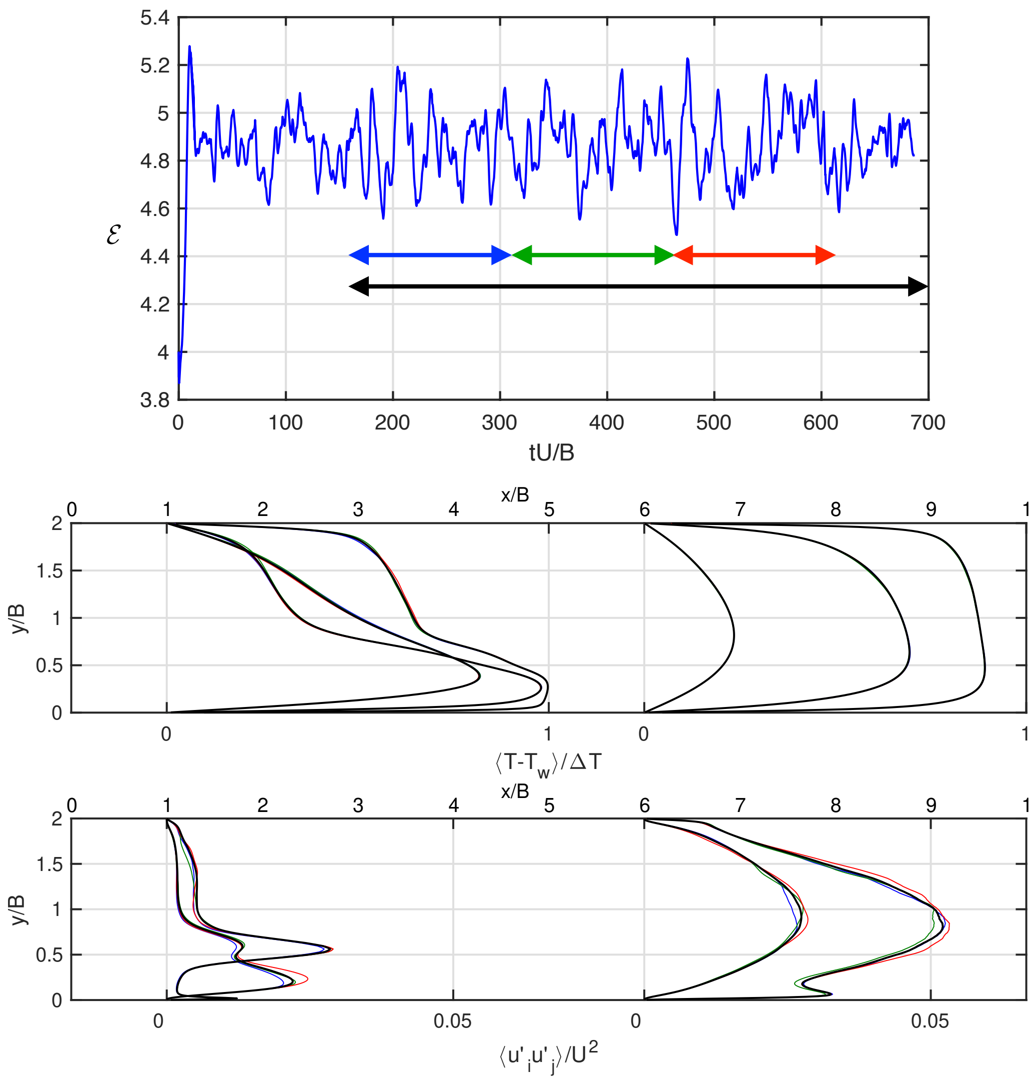

Figure 5: T4000 Case : Statistical convergence - Top : Time-history of the Enstrophy $\mathcal{E}$ in the whole domain. The arrows indicate the averaging windows. Middle and Bottom: Temperature profiles at $Pr = 1 - 0.1 - 0.01$ and velocity fluctuation profiles averaged over different averaging windows (the colors correspond to the averaging windows of the top figure).

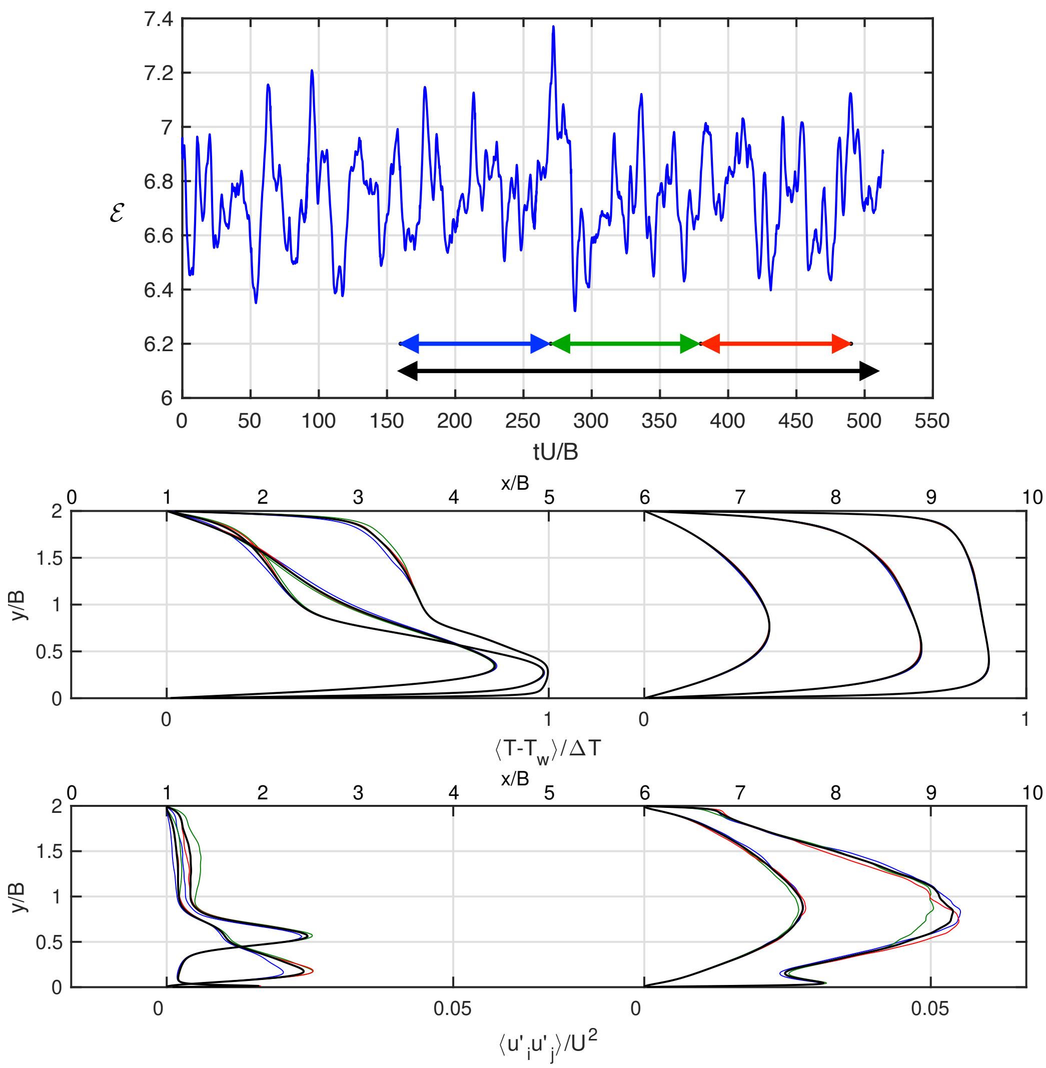

Figure 6: T5700 Case: Statistical convergence - Top : Time-history of the Enstrophy $\mathcal{E}$ in the whole domain. The arrows indicate the averaging windows. Middle and Bottom: Temperature profiles at $Pr = 1 - 0.1 - 0.01$ and velocity fluctuation profiles averaged over different averaging windows (the colors correspond to the averaging windows of the top figure).

are smoothed as the Prandtl decreases. At $Pr = 1$, the core jet at T_j is well visible and only starts to diffuse around $x/B = 4$ when the flow becomes turbulent. At $Pr = 0.01$, the temperature already diffuses in the vertical jet so that no clear region of T_j is visible. Only very weak turbulent fluctuations can be observed. The thermal boundary layers on the bottom wall, being at T_w, are also much thicker at the lowest Pr, even at the stagnation point. The $Pr = 0.1$ case is obviously the intermediate between the two other cases: a core at the jet temperature can be observed even after the impingement and turbulent structures are well visible, yet all the gradients are much smoother compared to the $Pr = 1$ case.

In the T4000 case (Fig. 8), the turbulent fluctuations in the jet are well visible at the inlet, in both the velocity and vorticity fields. This results in an enhanced mixing of the jet which is already well-mixed after the impingement, at around $x/B = 3$. Consequently, for the temperature at $Pr = 1$, the isothermal core at T_j does not penetrate as far as in the L4000 case, as it mixes faster. At lower Pr, the differences are less pronounced because of the smoothing effect by the higher molecular diffusivity. In the T5700 case (Fig. 9), the flow field is very similar to the T4000 case, even though the gradient are sharper because of the higher Re. Visually, on the velocity magnitude field, the growing wall-jet is more discernable for a longer distance after impingement. The vortical structures are obviously smaller and some Kelvin-Helmholtz-like roll-up are visible in the high shear regions of the vertical jet. The temperature fields are qualitatively very similar in the T4000 and T5700 cases.

Three-dimensional visualizations of the turbulent structures using the λ_2 criterion of Jeong and Hussain [27] are shown in Fig.10 for the three cases. In the L4000 case, large coherent spanwise vortices due to the Kelvin-Helmholtz instabilities are visible in the jet shear-layers. These vortices are eventually unstable and lead to the transition of the wall-jet. This transition is also followed by the transition of the bottom wall boundary layers and the generation of near-wall vortical structures. Those coherent spanwise vortices are not visible in the turbulent T4000 and T5700 cases, where smaller less coherent vortices populate the high-shear region of the jets. The other important difference between the laminar and turbulent cases is the presence of elongated quasi-streamwise vortices very close to the bottom wall in the stagnation region of the turbulent cases. Those vortices span across both sides of the stagnation line. Beaubert and Viazzo [28] observed similar vortices in their LES but did not analyze their effect in depth. Sakakibara et al.

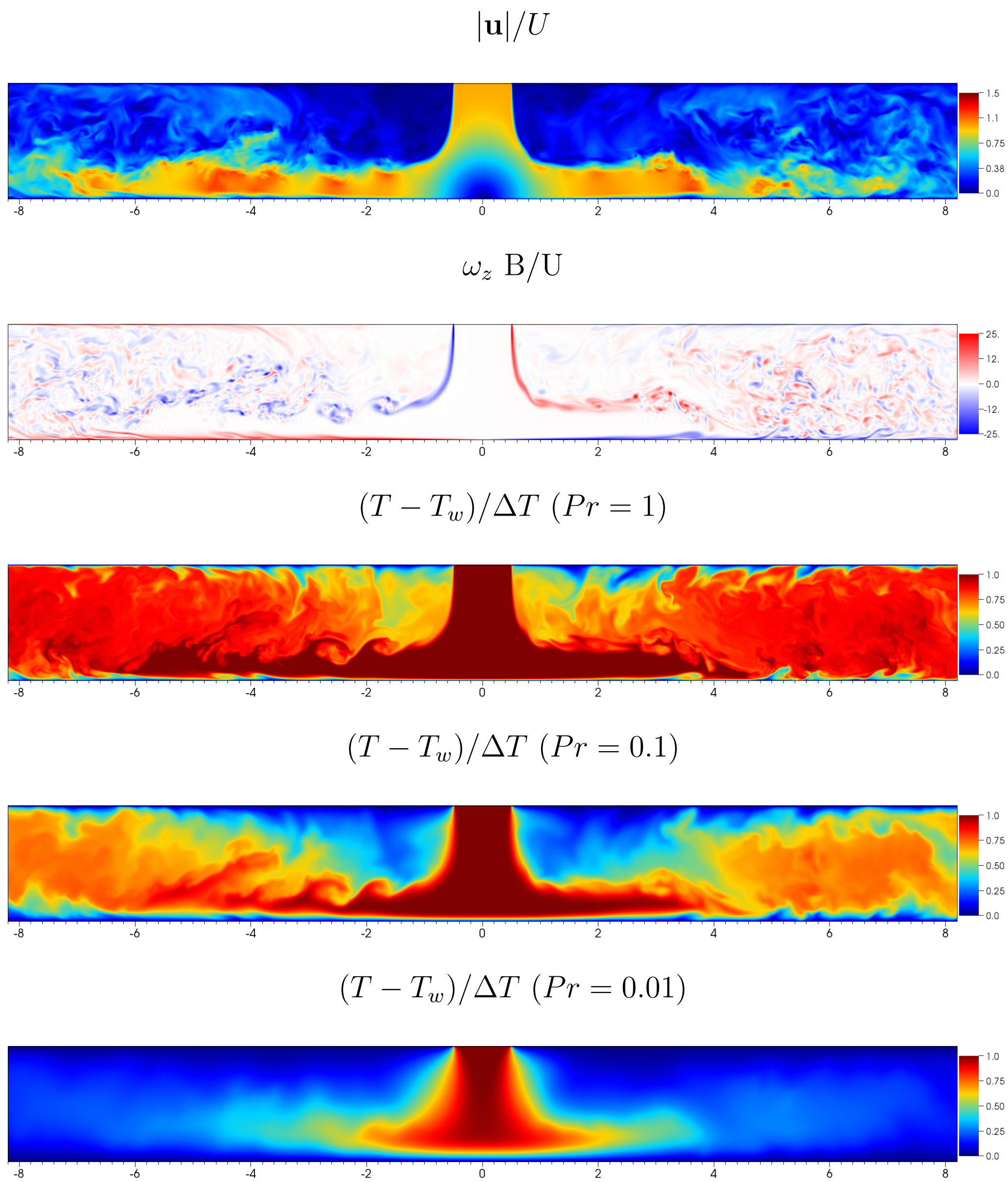

Figure 7: L4000 Case : visualizations of the instantaneous flow field in an arbitrary $x - y$ plane. Only the region $|x|/B < 8$ is shown.

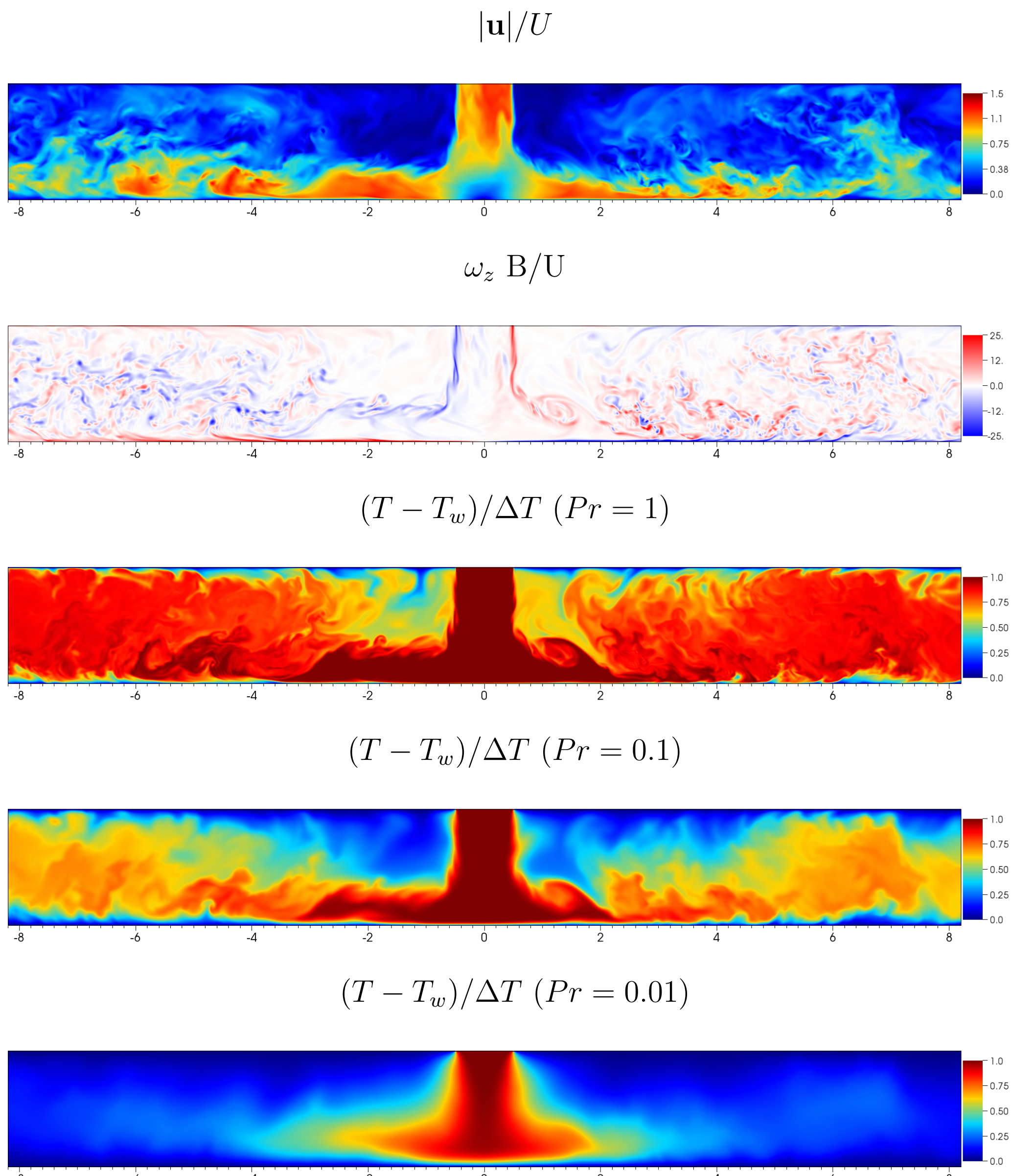

Figure 8: T4000 Case : visualizations of the instantaneous flow field in an arbitrary $x - y$ plane. Only the region $|x|/B < 8$ is shown.

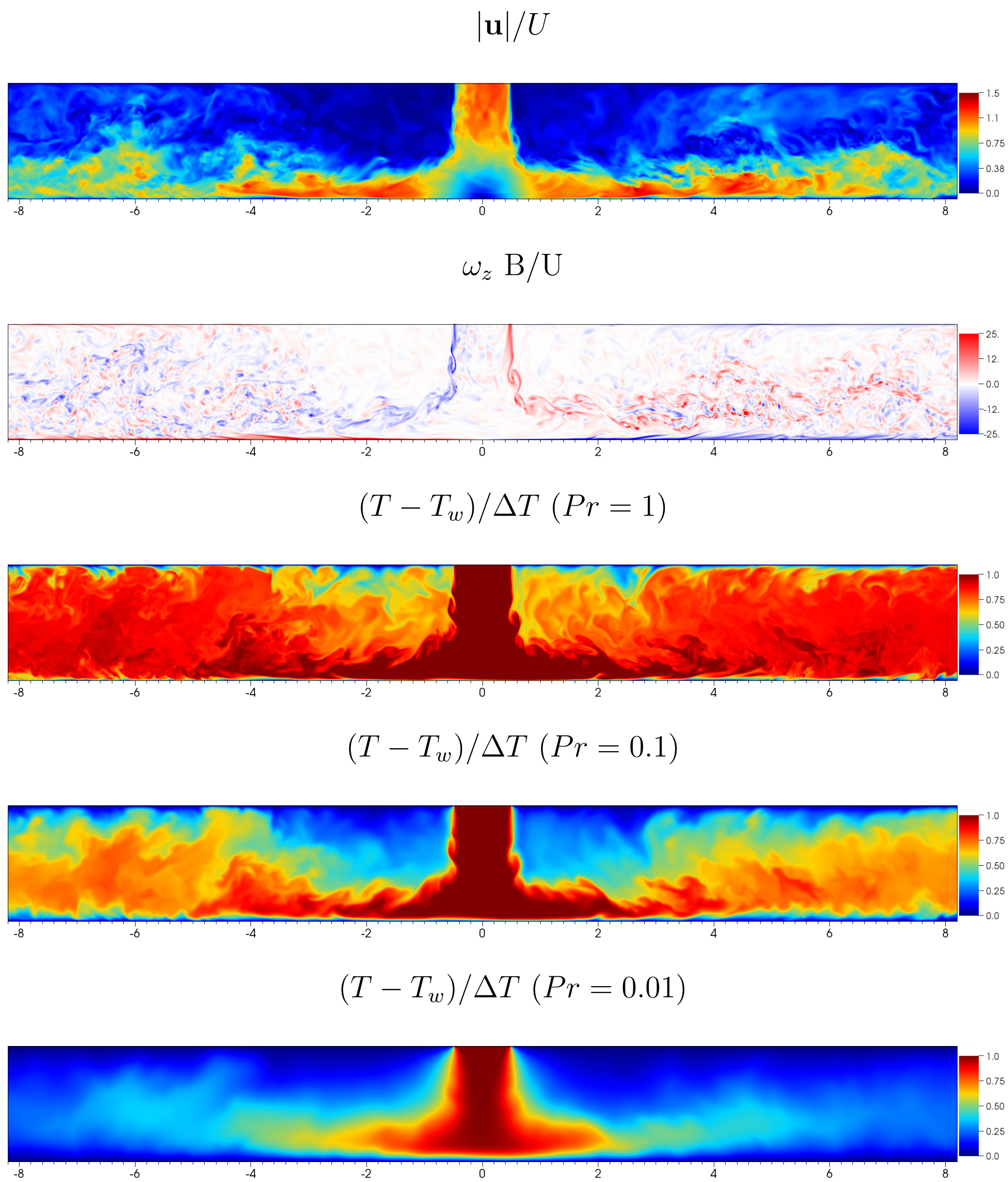

Figure 9: T5700 Case : visualizations of the instantaneous flowfield in an arbitrary $x - y$ plane. Only the region $|x|/B < 8$ is shown.

[19] experimentally studied those vortices using PIV in the symmetry plane of the jet. They showed that they are arranged in counter-rotating vortex pairs and that the wall-normal velocity they induce increases the mixing and, hence, the wall fluxes. Here, it can be observed that those vortices are very long and only disappear where the boundary layer transition to turbulence. Since, they are not present in the laminar inlet case, this shows that they are produced by vortical structures present in the jet which are stretched by the intense velocity gradient between the low-speed stagnation region and the high speed jet. This stretching process also tends to align those vortices with the streamwise direction. Therefore, those structures can only be observed when the jet is turbulent, either because it is initially turbulent or because the aspect ratio is large enough to allow a laminar jet to transition, as observed by Sakakibara et al. [19, 20]. Since these structures are due to the stretching in two exactly opposite directions, they are not observed in round jets (Hadziabdic and Hanjalic [14] and Dairay et al. [16]). Similar structures were also observed in the interaction of turbulent vortex pairs with a wall (Bricteux et al. [29]), where the stagnation region on the wall between the vortex pair is very similar to an impinging plane jet.

The effect of the elongated vortices in the stagnation region can been seen in the local instantaneous streamwise friction coefficient $C_{f,x} = \frac{\tau_{w,x}}{\frac{1}{2}\rho U^2}$ (Fig. 11) and Nusselt numbers $Nu = \frac{q_w}{\frac{k}{B}\Delta T}$ (Figs. 12, 13 and 14, for $Pr = 1$, 0.1 and 0.01 respectively). Those streamwise vortices generate elongated streamwise streaks which can be seen in both the wall shear-stress and the heat fluxes across the stagnation region for $|x|/B < 3$. These streaks are obviously not present in the L4000 case where the stagnation line is also straight and unperturbed, and where the boundary layers are laminar. In the L4000 case, however, strong spanwise structures can be observed, even leading to local recirculation around $x/B = 3.75$. They are maybe related to the Kelvin-Helmholz instability of the shear layer of the jet which produces strong spanwise vortices. In the L4000 case, the transition of the boundary layers occurs around $|x|/B = 5$, where small scale perturbations of wall-friction and heat flux are seen to appear. In the turbulent T4000 and T5700 case, a transition occurs between $|x|/B = 3$ and 4 where the long streaks break down into shorter structures. The turbulent regions $|x|/B > 6$ are qualitatively similar in both L4000 and T4000 cases.

Regarding the heat transfer, the elongated streamwise vortices significantly increase the heat transfer locally since the maximum local heat flux in

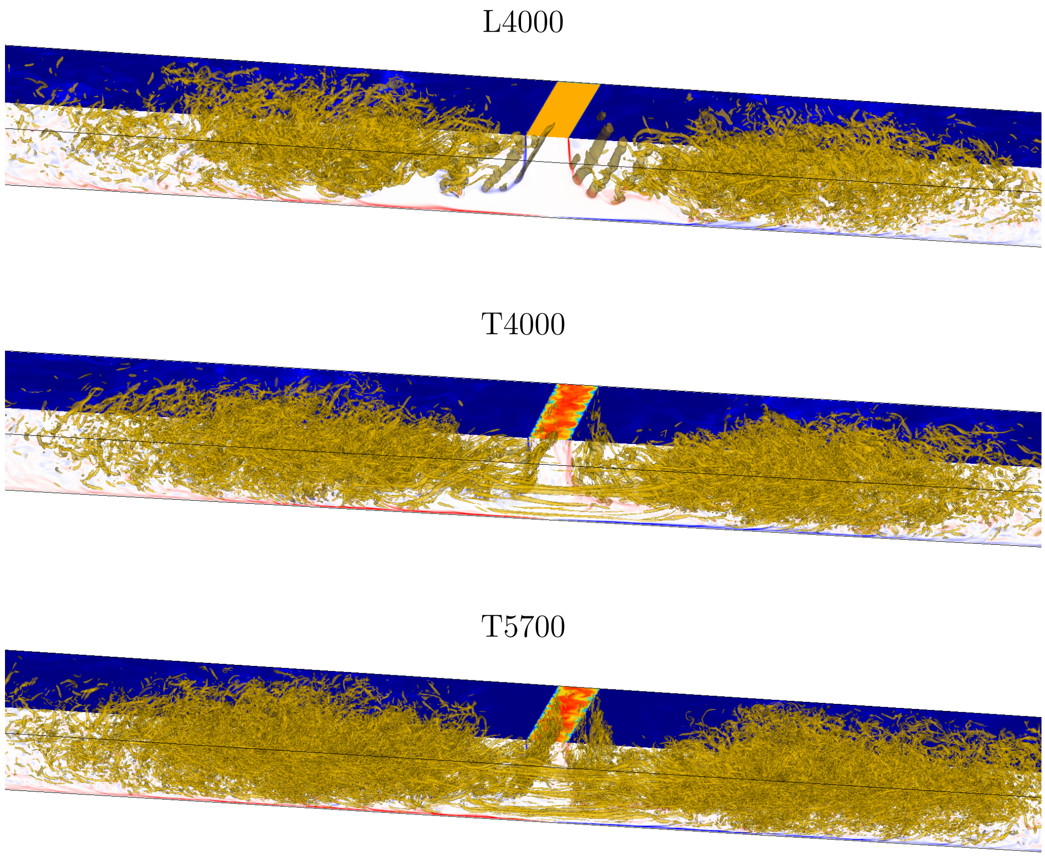

Figure 10: Instantaneous 3D visualizations using an isosurface of the λ_2 criterion (view from below through the bottom wall). The ω_z component is also shown in a $x - y$ plane close to the far side of the domain and the velocity magnitude in a $x - z$ plane close to the top wall.

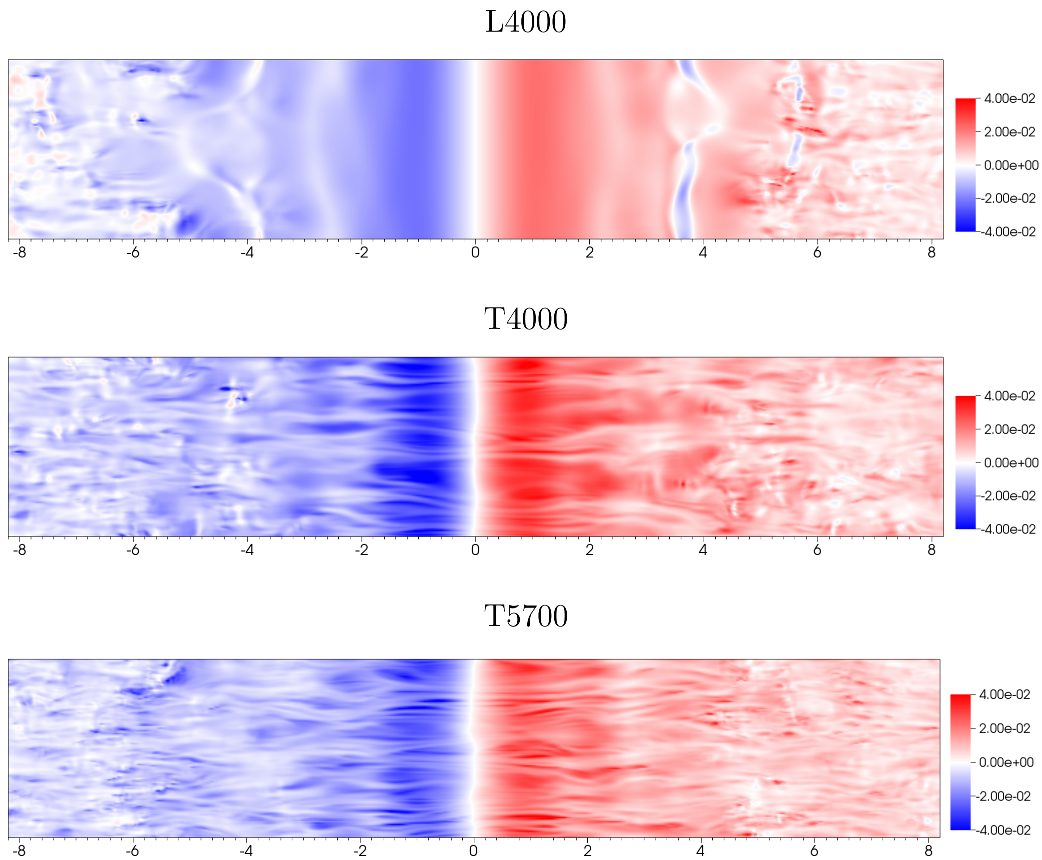

Figure 11: visualizations of the instantaneous friction coefficient $C_{f,x} = \frac{\tau_{w,x}}{\frac{1}{2}\rho U^2}$ on the bottom wall.

the elongated streaks in T4000 are also twice higher than the laminar heat flux obtained in L4000 (Figs. 12, 13 and 14). As the Pr number is lowered, the Nu values are decreased and the turbulent fluctuations are smoothed. Yet, the elongated structure are still present for Pr as low as 0.01, but they are much wider than at $Pr = 1$. At $Pr = 0.01$, the Nu fluctuations in the turbulent region $|x|/B > 6$ are very small compared to the other cases where intense heat flux spots can still be observed for $|x|/B > 6$.

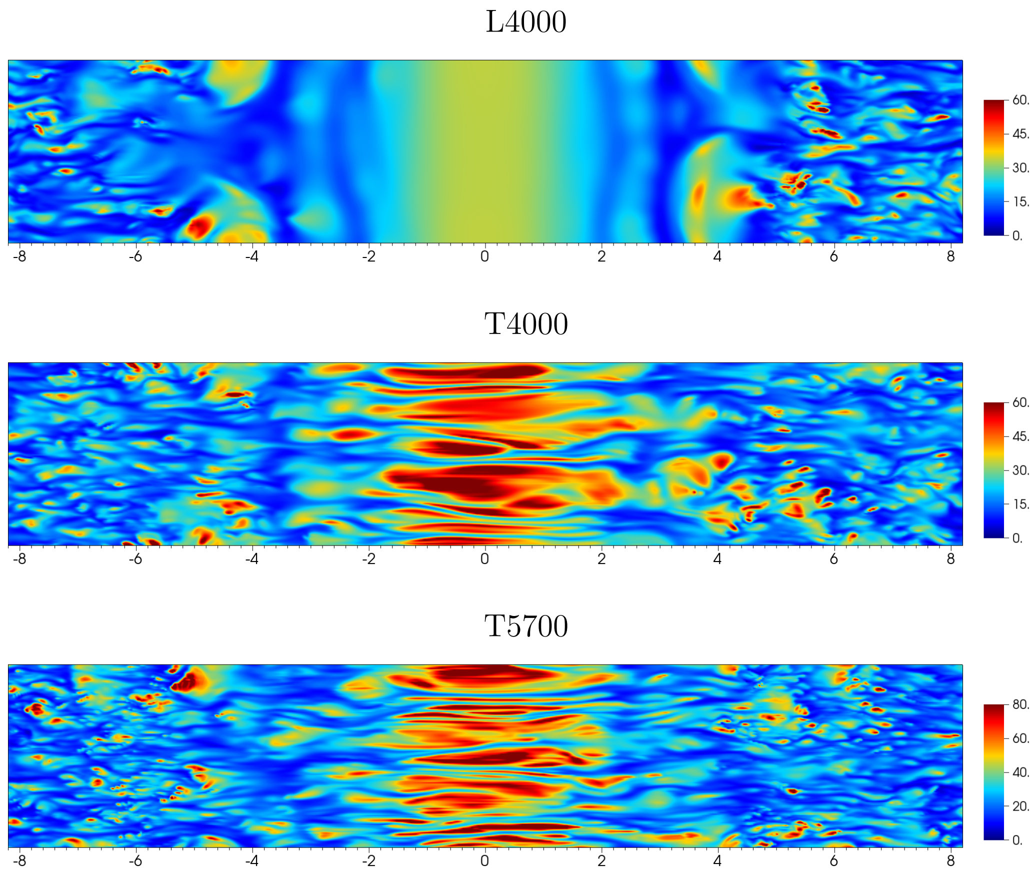

Figure 12: visualizations of the instantaneous Nusselt number $Nu = \frac{q_w}{\frac{k}{B}\Delta T}$ at $Pr = 1$ on the bottom wall.

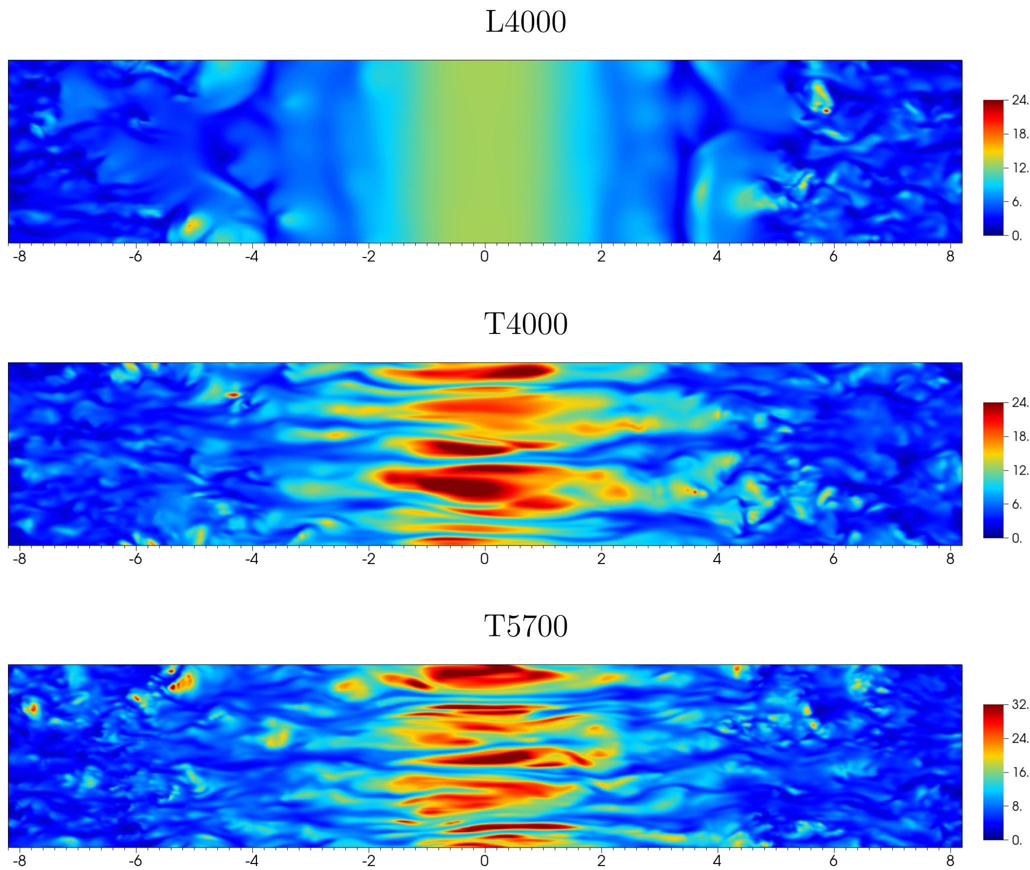

Figure 13: visualizations of the instantaneous Nusselt number $Nu = \frac{q_w}{\frac{k}{B}\Delta T}$ at $Pr = 0.1$ on the bottom wall.

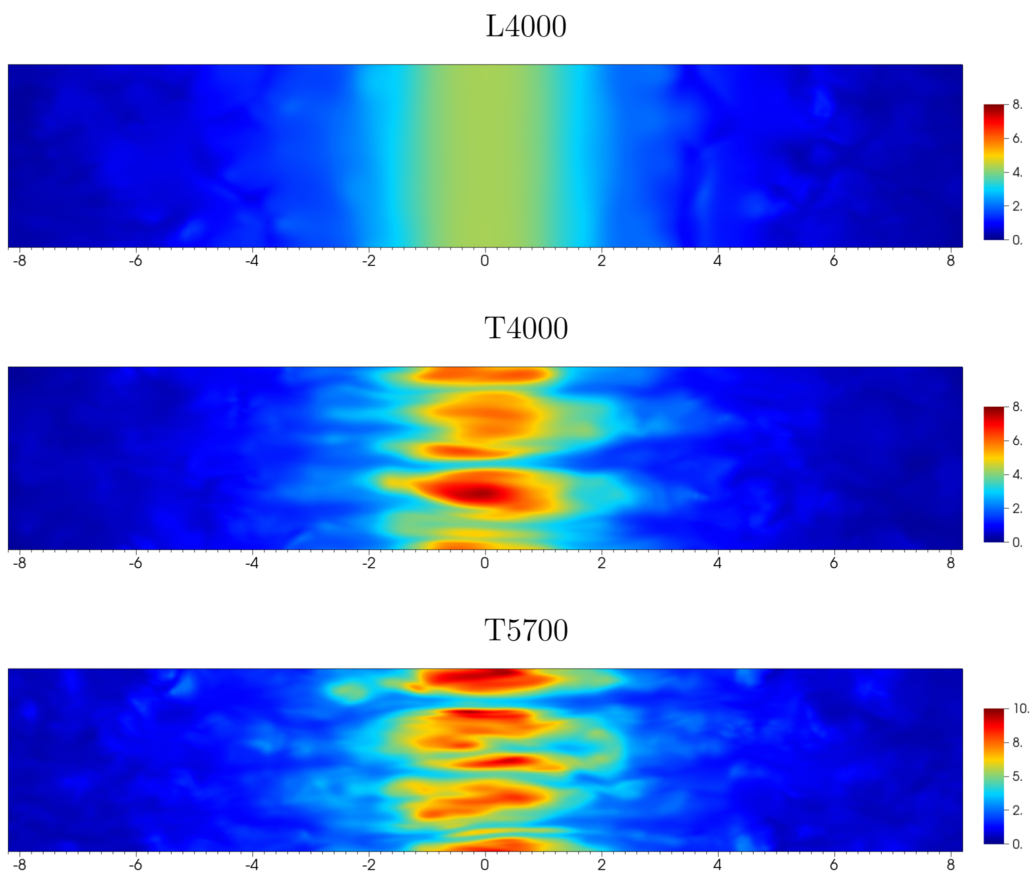

Figure 14: visualizations of the instantaneous Nusselt number $Nu = \frac{q_w}{\frac{k}{B}\Delta T}$ at $Pr = 0.01$ on the bottom wall.

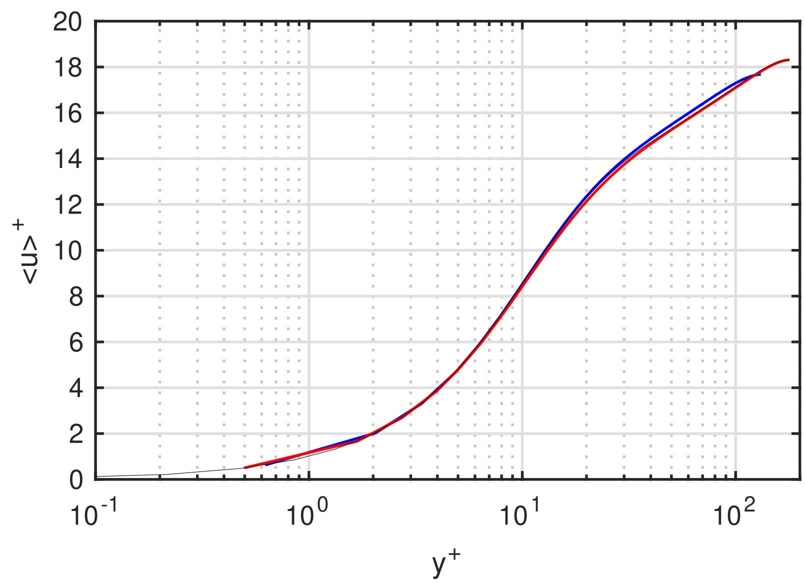

Figure 15: Auxiliary channel flow: mean velocity profile : $Re = 4000$ (blue), $Re = 5700$ (red) and $Re_\tau = 180$ by Moser et al. [26] (thin black).

5. Mean flow statistics

First, the mean flow statistics of the auxiliary channel flow simulations, which are used as inflow boundary condition, are briefly presented. Second, the statistics of the impinging jet simulations are then described.

5.1. Auxiliary channel flow

The channel flows results are presented in the conventional channel flow axes, with x the streamwise, and y the wall-normal directions, whereas the actual jet is blown along the $-y$ direction.

The mean velocity profiles of the auxiliary channel flows are shown in Fig. 15. As previously mentioned, the $Re = 4000$ and 5700 corresponds to $Re_\tau = 133$ and 181 respectively. The DNS at $Re_\tau = 180$ by Moser et al. [26] is also shown on the plots for validation. The mean profile obtained at $Re = 5700$ collapses very well with the reference DNS [26]. Due to low Re effects, the $Re = 4000$ profile is slightly higher than the other profiles for $y^+ > 50$.

The velocity RMS fluctuations are shown in Fig. 16 and the different mean stress contributions in Fig. 17. The near-wall peak of fluctuations is slightly smaller in the $Re = 5700$ simulation than in the reference DNS of

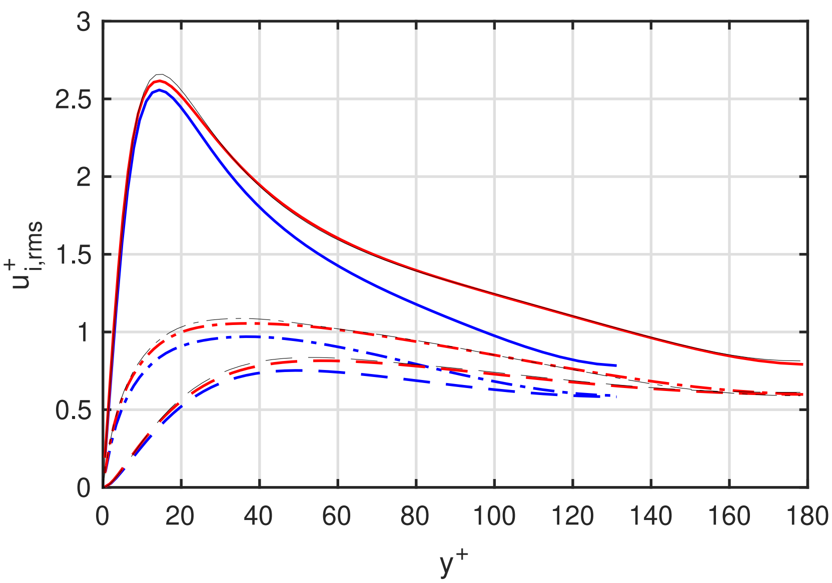

Figure 16: Auxiliary channel flow: fluctuation profiles: $\langle u \rangle_{rms}$ (solid), $\langle v \rangle_{rms}$ (dash-dot), and $\langle w \rangle_{rms}$ (dash) at $Re = 4000$ (blue), $Re = 5700$ (red) and $Re_\tau = 180$ by Moser et al. [26] (thin black).

Moser et al. [26]. The curves otherwise collapse in the bulk of the channel. For the turbulent stress, the discrepancy in the center of the channel is due to the difference of Re_τ between the simulations: the actual Re_τ value of Moser et al. [26] is slightly smaller than 180. In the $Re = 4000$ case, because of the lower Reynolds number, the fluctuations are smaller throughout the channel when normalized in inner ($^+$) variables.

The good agreement between the $Re = 5700$ simulation and the DNS by Moser et al. [26] validates the present channel flow simulations which are thus suitable as fully-developed turbulent inflow conditions for the impinging jet.

5.2. Impinging jet

First, in order to provide a general view of the mean flow, the streamlines of the mean flow are shown in Fig. 18. The full right half of the computational domain is displayed to show its extents, whereas zooms on the jet region are presented in Fig. 19. In all three cases, the vertical jet, which is then deflected, is clearly visible as well as the recirculating region next to the jet. A small secondary recirculation can also be observed in Fig. 19. The

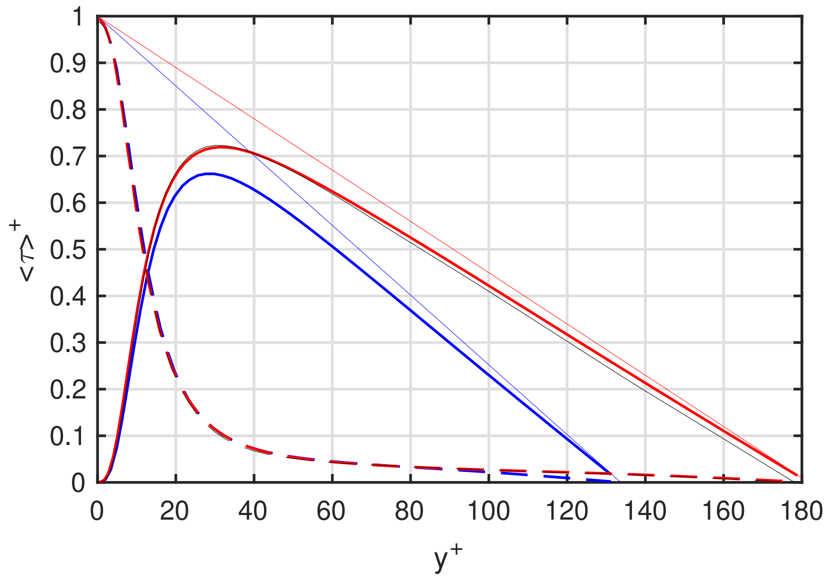

Figure 17: Auxiliary channel flow: stress profiles: $\langle\tau\rangle_{turb}$ (solid), $\langle\tau\rangle_{visc}$ (dash), and $\langle\tau\rangle_{tot}$ (thin solid) at $Re = 4000$ (blue), $Re = 5700$ (red) and $Re_\tau = 180$ by Moser et al. [26] (thin black).

deflected jet starts to spread significantly at around $x/B = 6$ and the flow reattaches on the upper wall around $x/B = 9.5$ at $Re = 4000$, and slightly further, around $x/B = 10$ at $Re = 5700$. Fig. 18 shows that the outflow boundary is located very far from the reattachment point which is thus not influenced by this boundary. It could even be expected that the domain could be shortened by placing the outflow boundaries at $|x|/B = 30$ without significantly influencing the flow. Yet, having a domain as short as $26B$, i.e $|x|/B < 13$, as used by Hattori and Nagano [21], would alter the size of the recirculating region, and thus the rest of the flow.

The averaged friction coefficient C_f on the bottom wall is shown in Fig. 20. The Cf curves start at zero at the stagnation point, reach a maximum close to $x/B = 1$ and then decrease to reach a plateau corresponding to the fully developed flow between the two walls. Yet, between $x/B = 4$ and 5 depending on the case, the curves exhibit a plateau, or at least a flatter region, before decreasing faster again. In the L4000 case, the end of the plateau is located at $x/B = 6$, which corresponds to the deceleration of the jet and the transition to turbulence of the thin boundary layers developing on the plate (as seen in Fig. 11). For the turbulent inlet at the same Reynolds

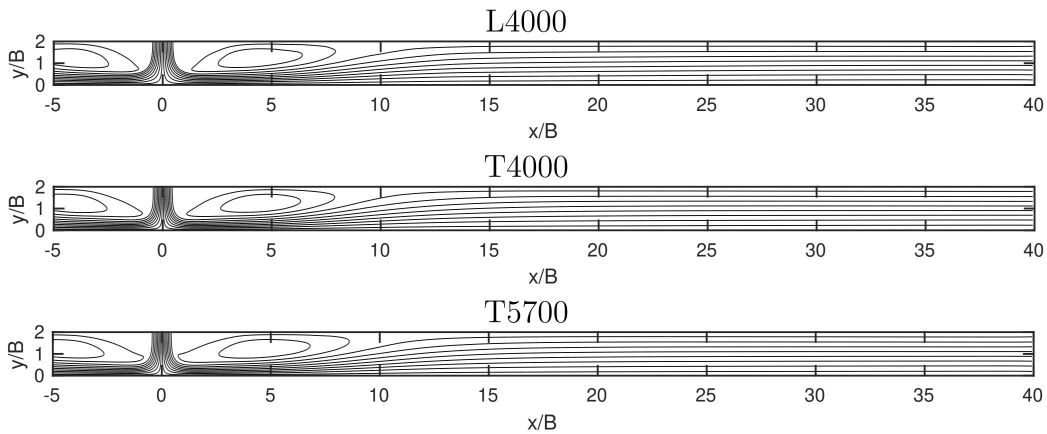

Figure 18: visualizations of the streamlines of the mean flow.

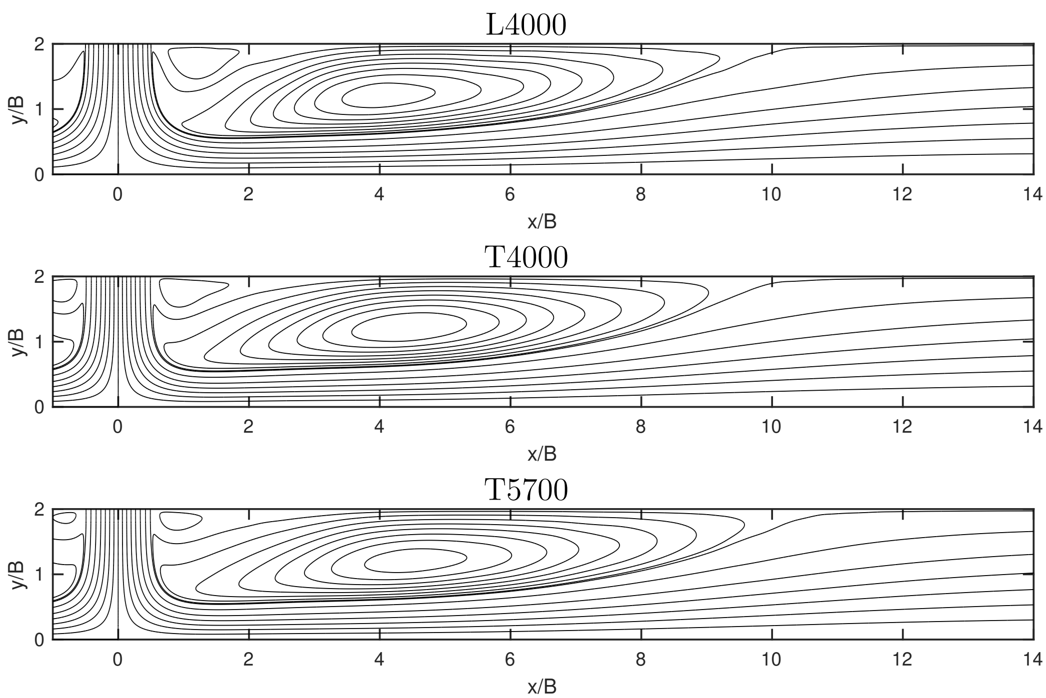

Figure 19: visualizations of the streamlines of the mean flow (zoom in the jet region).

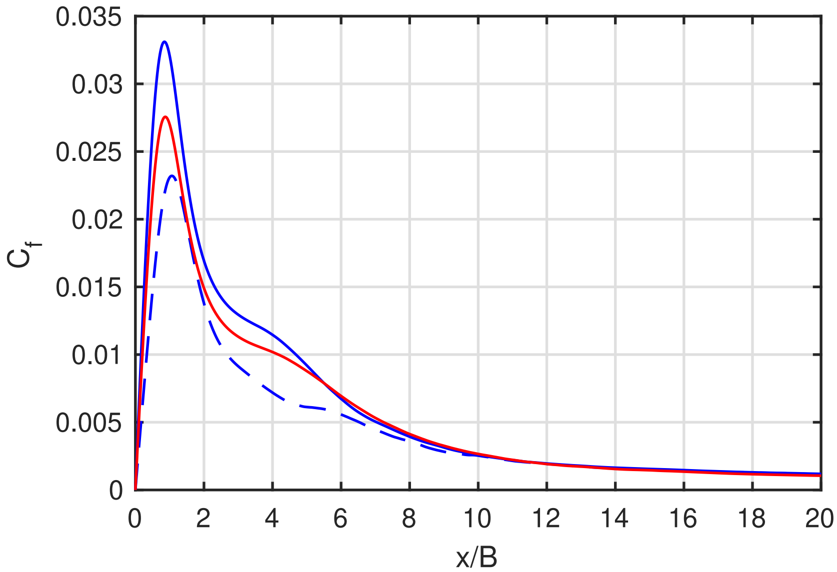

Figure 20: Mean friction coefficient $C_{f,x} = \frac{\tau_{w,x}}{\frac{1}{2}\rho U^2}$ on the bottom wall: L4000 (blue dash), T4000 (blue solid) and T5700 (red).

number (T4000), the friction coefficient is much larger in the whole region before $x/B = 6$, where the curves come closer to each other. This increased C_f is due to the increased mixing by the long streamwise vortices discussed earlier. The curves almost collapse when the boundary layers transition and the friction then does not depend on the initial state of the jet. When the Re number is increased (T5700), the C_f decreases, as expected in boundary layers, but the shape of curve is globally similar to the $T4000$ case, even though the bump is located slightly further, around $x/B = 5$, compared to 4 in the T4000 case.

The heat flux at the lower wall is presented in the form of the mean Nusselt number Nu in Fig. 21. For the Nusselt number at $Pr = 1$ in the L4000 case, the laminar-turbulent transition leads to a secondary peak whose maximum is located at $x/B = 6$. However, in the T4000 case, the secondary maximum is not present because the Nu values before $x/B = 6$ are significantly increased with a small plateau around $x/B = 4$. Yet, the L4000 and T4000 curves collapse almost exactly for $x/B > 6$. Again, this increase is due to the enhanced mixing by the vortical structures present near the bottom wall. The plateau is located where these structures starts to breakdown. Then, when the boundary layers have transitioned, the heat flux is identical in both

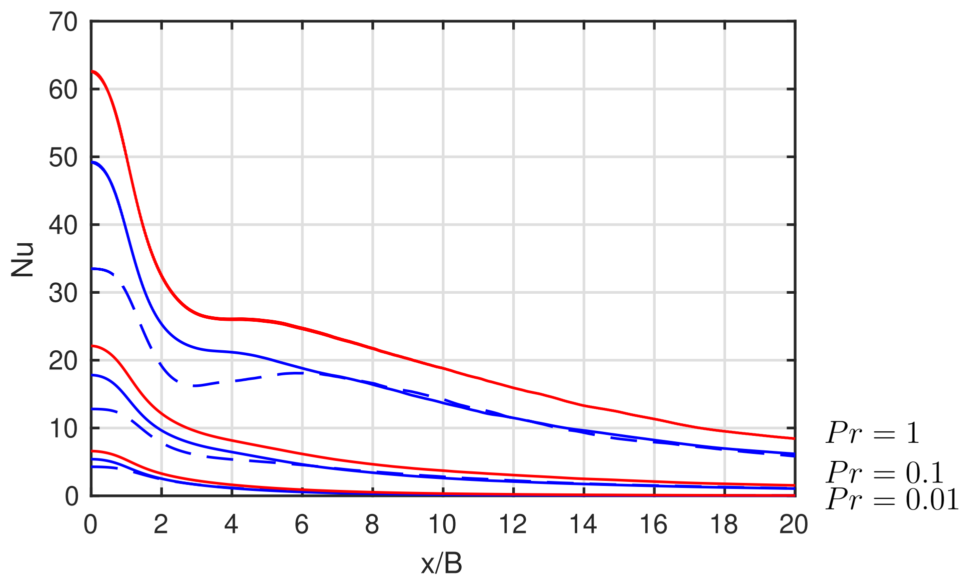

Figure 21: Mean Nusselt number $Nu = \frac{q_w}{\frac{k}{B}\Delta T}$ on the bottom wall: L4000 (blue dash), T4000 (blue solid) and T5700 (red).

laminar and turbulent cases. The T5700 yield higher Nu values but with a very similar shape as the T4000 case, even though the plateau then ends around $x/B = 4.5 - 5$.

This secondary maximum of the Nusselt number is a well-known characteristic of impinging jets, as it has been observed experimentally [10] and numerically, using DNS, by Jaramillo et al. [22] in plane jets or by Dairay et al. [16] in round jets. Similarly to the present results, Hattori and Nagano [21] did not observed such a secondary peak in their DNS at $Re = 4560$ with $H/B = 2$ as they used a fully developed turbulent inlet. However, they observed it when they decreased significantly the aspect ratio to $H/B = 0.5$. The secondary maximum was already linked to the vortical structures in the transition region of their round jets by Hadziabdic and Hanjalic [14] and Dairay et al. [16]. The latter studied in details the mechanism by which local vortical structures lead to this increase of heat transfer by bringing outer fluid closer to the wall, and thus increasing the local temperature gradient. Here, the one-to-one comparison between the laminar and the turbulent inlets, allows to clearly identify how the vortical structures in the stagnation region affect the heat transfer and the presence of the secondary maximum or not.

It can be observed in Fig. 21 that the secondary peak is not present in the Nu profiles at lower Pr, in all three cases. This is due to the fact that, at low Pr, the enhancement of the heat flux by the turbulence is not sufficient to compensate for its decrease due to the diffusion of the thermal layer. However, an increase of Nu close to the stagnation region can be seen between the L4000 and the T4000 at $Pr = 0.1$ and also at $Pr = 0.01$. There is thus still some heat flux enhancement by the wall structures, before the temperature fluctuations are smoothed out by the high molecular diffusivity, as already observed in the local values in Fig. 14. When Re is increased, as in the T5700 case, the shape of the curve in not modified but the Nu values increase, as expected in forced convection problems.

Shadlesky [30] proposed an expression of the stagnation Nusselt number Nu_0 in laminar 2D jets which is

$$Nu_0 = 0.505 Re^{0.5} Pr^{0.4}. \tag{1}$$

The stagnation Nusselt numbers of the present simulations are shown in Fig. 22. It can be seen that the Nu_0 of the L4000 simulation at $Pr = 1$ and 0.1 are quite close to the relation of Shadlesky [30]. The Nu_0 at $Pr = 0.01$ is however significantly smaller than the predicted value. The turbulent cases T4000 and T5700 can be used to fit a similar relation for the turbulent cases. Since it can be observed that the scaling is different at low Pr , the fit is performed separately for $0.1 \leq Pr \leq 1$ and $0.01 \leq Pr \leq 0.1$:

$$Nu_0 = \begin{cases} 0.234 Re^{0.65} Pr^{0.45} & \text{if } 0.1 \leq Pr \leq 1 \\ 0.460 Re^{0.59} Pr^{0.52} & \text{if } 0.01 \leq Pr \leq 0.1 \end{cases} \tag{2}$$

This fit is also displayed in Fig. 22. It is interesting to note that the Re and Pr exponents are very close at low Pr, so that Nu_0 essentially only depends on the Peclet number $Pe = Re\,Pr$ at low Prandtl, as considered in most low Prandtl correlations.

The mean velocity profiles at various stations are plotted in Fig. 23. The mean velocity profiles of the L4000 simulation show the potential core at $x/B = 1$ and 2 which is completely diffused at $x/B = 4$. The recirculating region is well visible with the reattachment taking place around $x/B = 9$, and a little further in the T5700 case. The mean profiles of the T4000 and T5700 are very close to each other. At $x/B = 1$, they do not exhibit a maximum in the shear layer and the shear layer is wider than in the L4000 case. Yet, the maximum velocity in the wall jet is larger in the turbulent

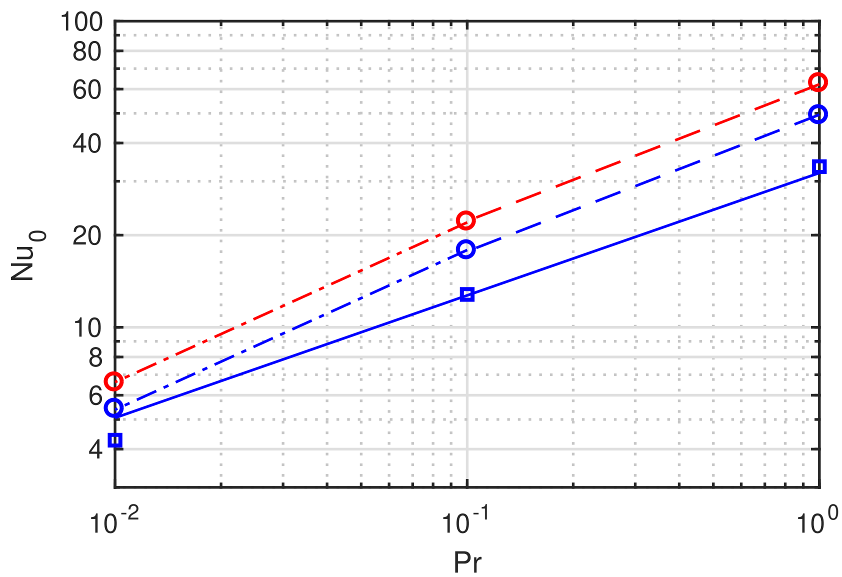

Figure 22: Mean Nusselt number at the stagnation points Nu_0 at $Re = 4000$ (blue) and 5700 (red), for the laminar (□) and turbulent (○) inlets. The relation by Shadlesky [30] (solid) and the fits between $Pr = [0.1; 1]$ (dash) and between $[0.01; 0.1]$ (dash-dot) are also drawn.

cases and very close to U. At around $x/B = 4$, the mean profiles of the L4000 and T4000 cases almost collapse except very close to the lower wall, since the wall shear stress is still different. At the last stations, $x/B = 6-9$, the maximum velocity of the T5700 case becomes larger than that of the $Re = 4000$ cases, as the wall jet diffuses more slowly.

Fig. 23 also presents the Root Mean Square (RMS) velocity $U_{rms} = \sqrt{\frac{2}{3}\langle k \rangle}$, where $\langle k \rangle = \frac{1}{2}(\langle u'^2 \rangle + \langle v'^2 \rangle + \langle w'^2 \rangle)$ is the Turbulent Kinetic Energy (TKE), whereas a few components of the Reynolds stress tensor for each case are shown in Fig. 24. Again, the T4000 and T5700 simulations yield very similar profiles even though the fluctuations of the T5700 case are smaller in the first stations ($x/B = 1-5$) then become larger in the center of the domain in the last stations ($x/B = 7-9$). Also the near-wall peak of U_{rms} diffuses more slowly in T5700 than in T4000.

In the L4000 simulation, the velocity fluctuations are first observed in the jet shear layer which becomes unstable. Another peak of U_{rms} then forms close to the lower wall at $x/B = 3$. This peak slightly increases but it is no longer visible at $x/B = 9$. From the profiles of the individual velocity

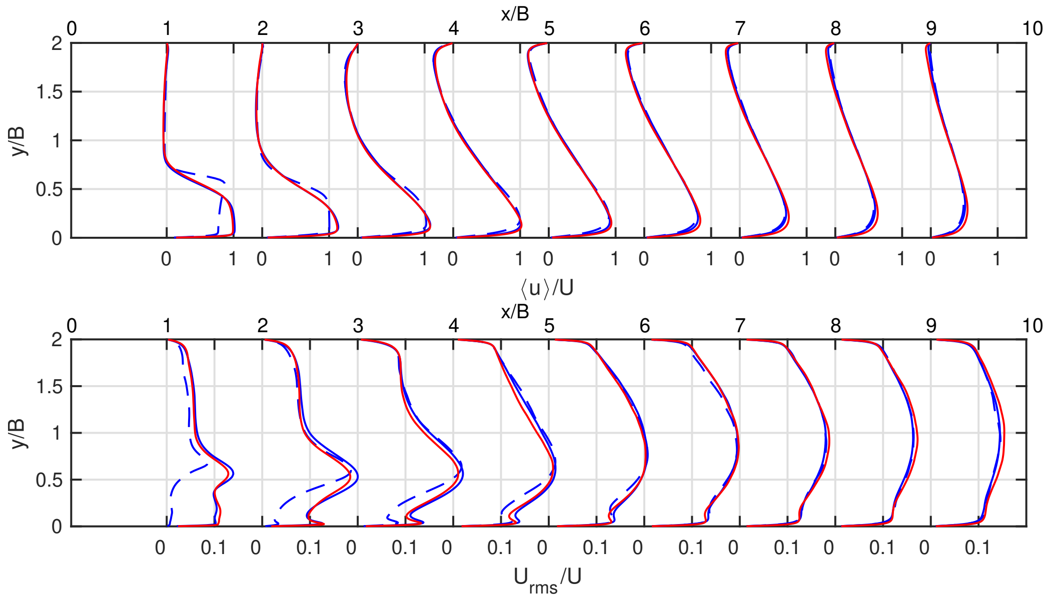

Figure 23: Mean axial velocity $\langle u\rangle/U$ (top) and RMS velocity $U_{rms}/U = \sqrt{\frac{2}{3}\langle k\rangle}/U$ (bottom): L4000 (blue dash), T4000 (blue solid) and T5700 (red).

fluctuations, it can be observed that the near-wall fluctuation peak is the strongest for the axial (u) velocity, which is typical of wall-bounded turbulent flows. Fig. 24 also shows the wall-normal turbulent stress $-\langle u'v'\rangle$. Like the RMS velocity, the turbulent shear stress first develops in the shear layer and then in the lower-wall boundary layer, where the fluctuation peak is also found.

In the turbulent T4000 and T5700 cases, the presence of significant fluctuations in the wall jet at the first station $x/B = 1$ is well visible but the profile of U_{rms} is relatively flat in the jet and has a maximum in the shear layer. At that station, close to the wall, a significant peak of spanwise velocity fluctuations can be observed in Fig. 24. This peak is related to the streamwise vortices. At the next station, $x/B = 2$, the spanwise peak decreases whereas a very strong peak of streamwise velocity fluctuations appears. This intense peak also leads to a near-wall peak in the U_{rms} profile. In the next stations, the peaks of fluctuations in the shear layer and near the wall diffuse and the fluctuation profiles become much flatter. Starting from $x/B = 6$, the fluctuation profiles from the laminar and turbulent cases are almost identical.

The mean temperature profiles are shown in Fig. 25. As already observed

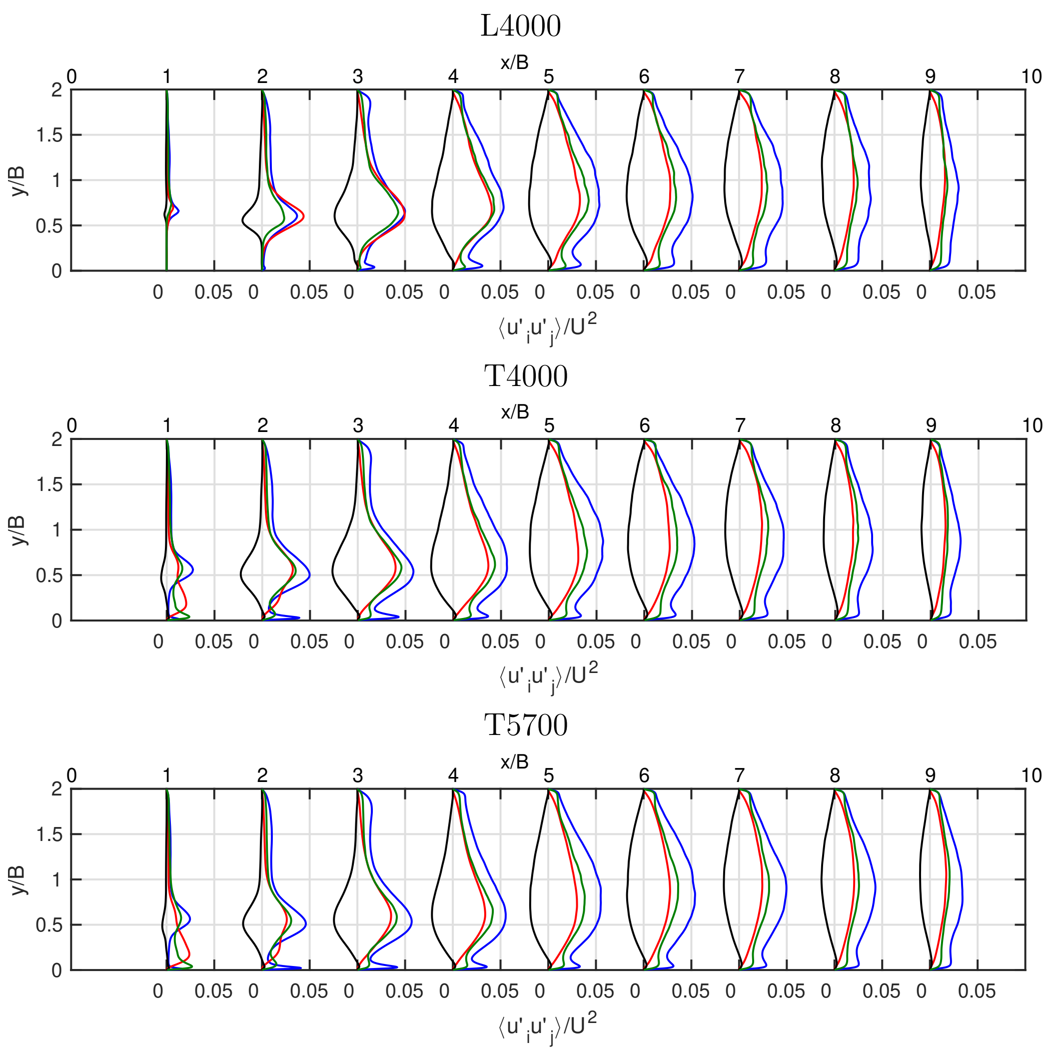

Figure 24: Mean velocity fluctuations $\langle u'^2 \rangle / U^2$ (blue), $\langle v'^2 \rangle / U^2$ (red), $\langle w'^2 \rangle / U^2$ (green) and turbulent stress $-\langle u'v' \rangle / U^2$ (black).

in Fig. 7-9, the low Prandtl case ($Pr = 0.01$) does not exhibit a core region at the jet temperature T_j, as the vertical jet is already much diffused. The $Pr = 1$ profiles, especially for L4000, exhibit an isothermal core at T_j. The temperature gradients at $Pr = 0.01$ are obviously much weaker than at higher Pr. At $x/B = 1$, the mixing region is well visible at $Pr = 1$, whereas at $Pr = 0.01$, the temperature decreases more gradually between the maximum in the jet towards the upper wall temperature. The temperature profiles in the three cases (L4000, T4000 and T5700) are all very similar, except at the first stations where the mixing layer is thinner in the L4000 case. The temperature profiles reach a developed shape much faster than the velocity, as the temperature profiles at $x/B = 7 - 8 - 9$ are very similar even though the flow is not reattached yet and thus clearly not fully developed. The temperature in the T5700 case is then slightly higher than in the other cases.

The temperature fluctuations profiles are given in Fig. 26. At the first station $x/B = 1$, in L4000, the temperature fluctuations are maximum in the recirculation bubble as the jet core is still laminar. On the contrary, in the turbulent simulations T4000 and T5700, a very strong peak of fluctuations is located near the bottom wall and is also related to the streamwise vortices. At $Pr = 1$, a peak of fluctuations is always present close to the upper wall. Another peak first develops in the mixing layer which progressively vanishes at stations further away from the stagnation point. In the L4000 simulation, the peak near the bottom wall develops as the boundary layers become turbulent. At the last stations, the profiles are almost symmetrical with a peak near each wall.. The profiles at $Pr = 0.1$ are essentially similar to those at $Pr = 1$ but with more diffused peaks. However, the fluctuations in the center, at $y/B = 1$, are slightly larger than at $Pr = 1$. At $Pr = 0.01$, the near-wall peaks are much less significant than at the two higher Pr. At the first station, there is a maximum of fluctuations in the middle of the recirculation region, while the turbulent cases (T4000 and T5700) also exhibit a near-wall peak. A peak in the mixing region only appears at further stations $x/B = 2$ and 3 and then quickly disappears. The near-wall peaks are very weak and the profiles at the last stations are almost flat, especially at $Re = 4000$.

The wall normal turbulent heat flux profiles $-\langle q \rangle_t = -\langle v'T' \rangle$ for the three cases are presented in Fig. 27. It can be observed that the largest turbulent flux is usually obtained at $Pr = 0.1$ and not 1, because there is a competition between the increase of the wall flux with Pr and a decrease of the fluctuations with Pr. The turbulent heat flux profiles are obviously closely

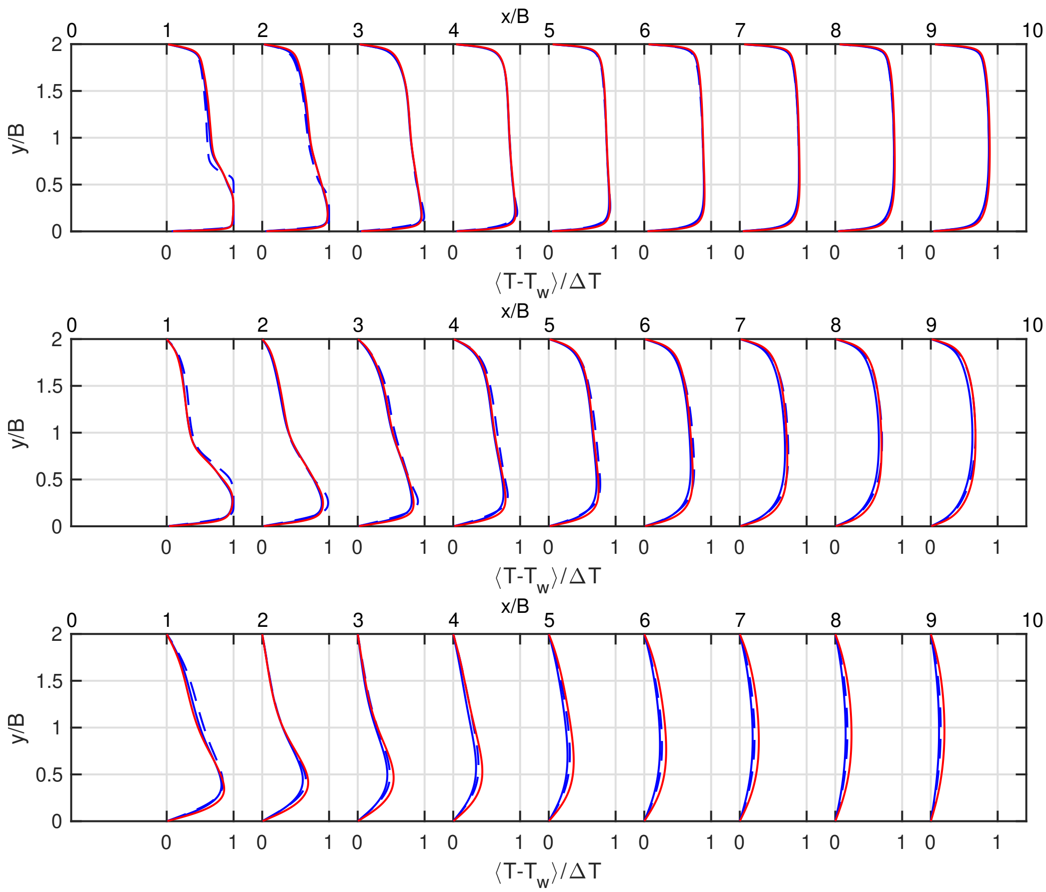

Figure 25: Mean temperature profiles $(\langle T \rangle - T_w)/\Delta T$ at $Pr = 1$ (top), 0.1 (middle) and 0.01 bottom): L4000 (blue dash), T4000 (blue solid) and T5700 (red).

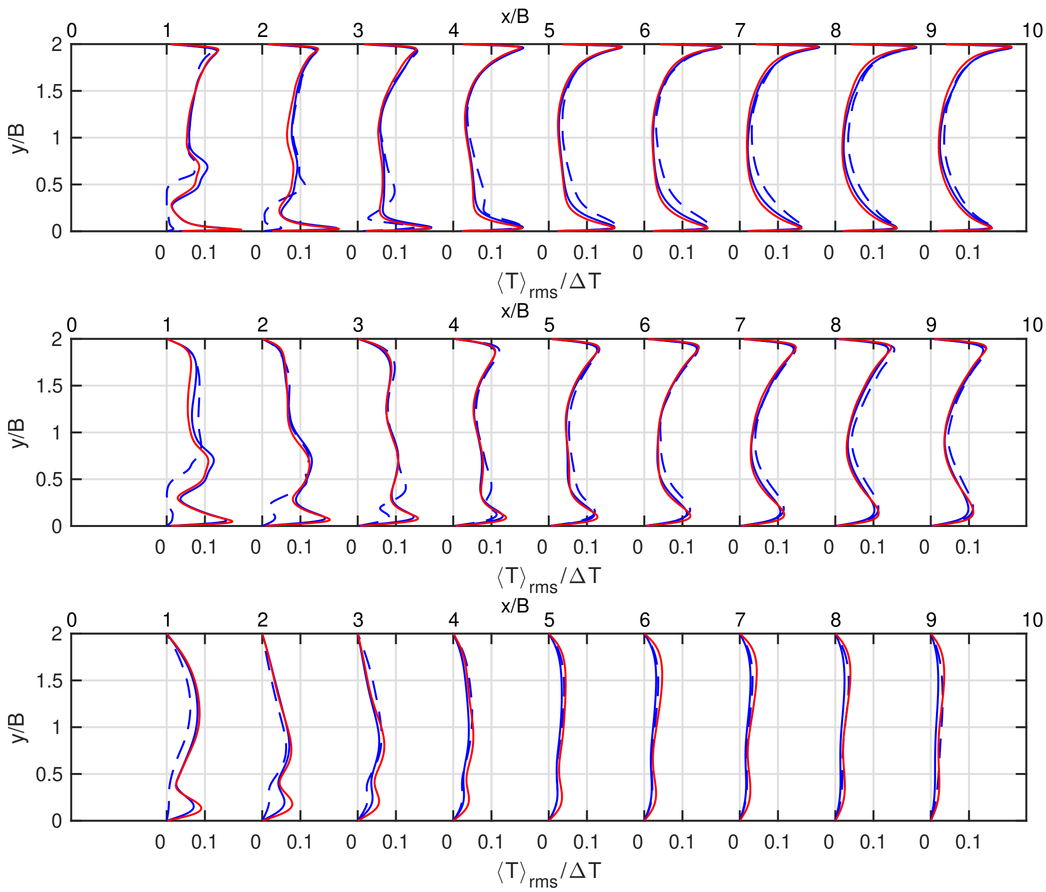

Figure 26: RMS temperature profiles $\langle T \rangle_{rms}/\Delta T$ at $Pr = 1$ (top), 0.1 (middle) and 0.01 (bottom): L4000 (blue dash), T4000 (blue solid) and T5700 (red).

related to the temperature fluctuations, and the presence of turbulent heat flux extrema is closely related to the fluctuation peaks observed in Fig. 26. Again, in the L4000 case, the turbulent flux is initially maximum in the mixing layer and then increases close to the walls. In the T4000 and T5700 cases, at $x/B = 1$, there is a strong heat flux maximum near the bottom wall and the turbulent heat flux in the mixing layer is larger than in L4000. In T4000 and T5700 at $Pr = 0.01$, the turbulent heat flux is slightly more intense in the mixing layer than in the recirculation region, also not at the same position than the maximum of fluctuations (Fig. 26). It can be seen that the peaks in the mixing layer at $x/B = 2$ are not located at the same height for the different Pr: it is further away from the lower wall as Pr decreases. Obviously, the near-wall maxima of the turbulent flux at $Pr = 0.01$ are much flatter and further away from the wall than at $Pr = 1$ and $Pr = 0.1$.

Figs. 28 to 30 show, for the three simulations, the relative importance of the turbulent and molecular wall-normal fluxes by plotting the profiles normalized by the local flux at the bottom wall. At $Pr = 1$, the turbulent flux is completely dominant and the molecular flux is only significant close to the wall and in the mixing layer at $x/B = 1$ for the laminar case. This is also the case at $Pr = 0.1$, and the only exception is again the mixing layer at $x/B = 1$ in the L4000 case. However, at Pr = 0.01, in the three simulations, the molecular flux dominates as it is always significantly larger than the turbulent flux.

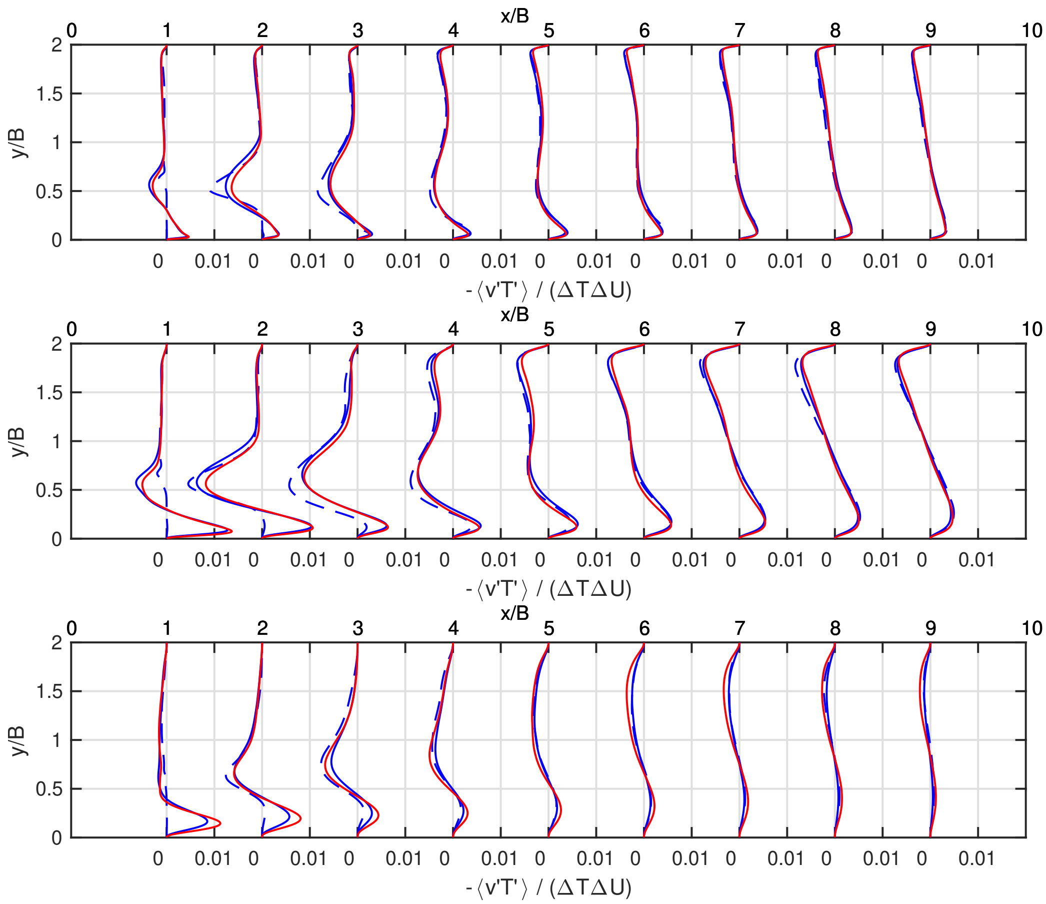

Figure 27: Mean turbulent heat flux profiles $-\langle v'T' \rangle/(\Delta T \Delta U)$ at $Pr = 1$ (top), 0.1 (middle) and 0.01 bottom): L4000 (blue dash), T4000 (blue solid) and T5700 (red).

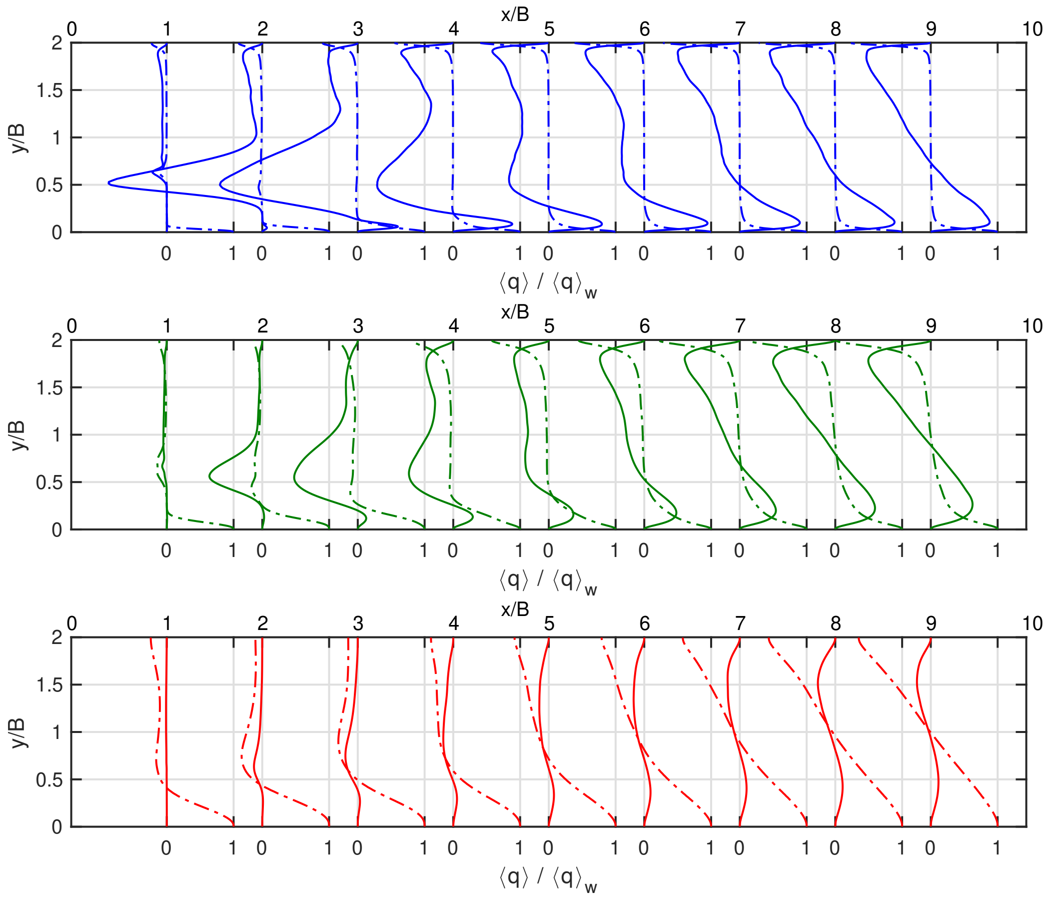

Figure 28: Case L4000 - Mean heat flux profiles normalized by the local heat flux on the bottom wall: $-\langle v'T'\rangle/\langle q\rangle_w$ (solid) and $k\langle\frac{\partial T}{\partial y}\rangle/\langle q\rangle_w$ (dash-dot) at $Pr = 1$ (blue), 0.1 (green) and 0.01 (red).

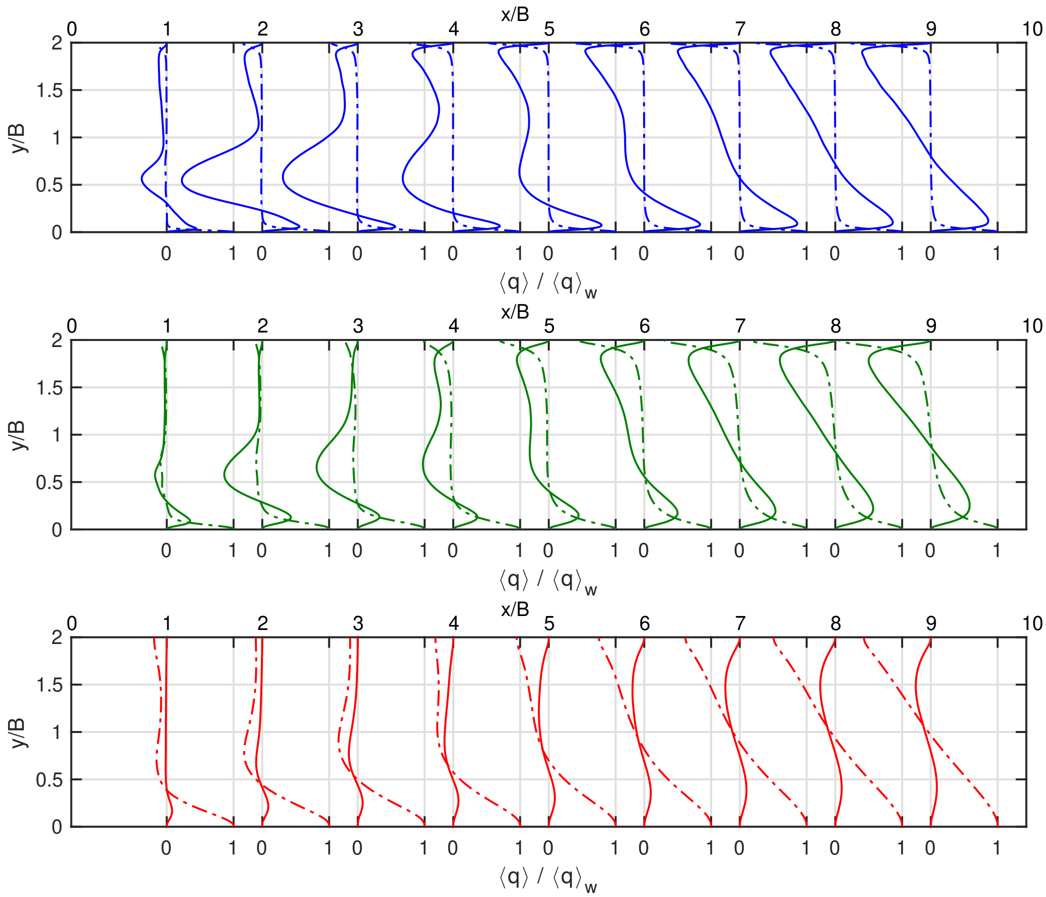

Figure 29: Case T4000 - Mean heat flux profiles normalized by the local heat flux on the bottom wall: $-\langle v'T' \rangle / \langle q \rangle_w$ (solid) and $k\langle \frac{\partial T}{\partial y} \rangle / \langle q \rangle_w$ (dash-dot) at $Pr = 1$ (blue), 0.1 (green) and 0.01 (red).

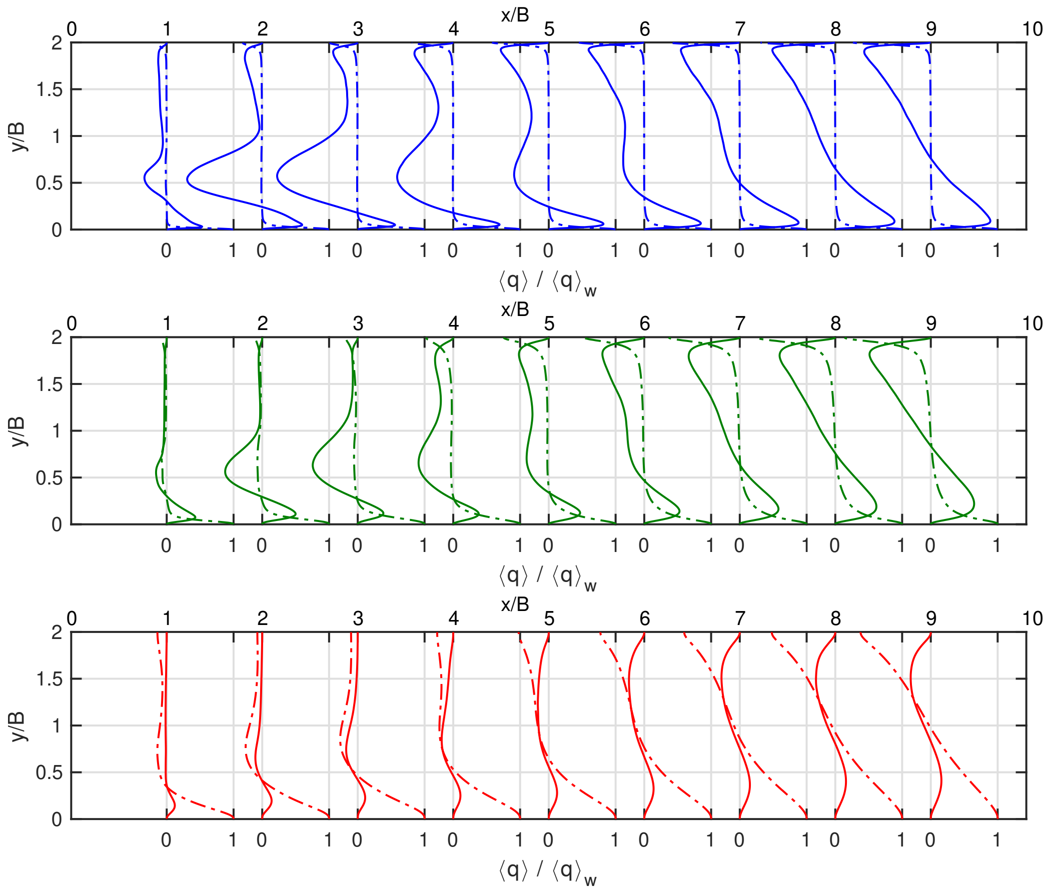

Figure 30: Case T5700 - Mean heat flux profiles normalized by the local heat flux on the bottom wall: $-\langle v'T'\rangle/\langle q\rangle_w$ (solid) and $k\langle\frac{\partial T}{\partial y}\rangle/\langle q\rangle_w$ (dash-dot) at $Pr = 1$ (blue), 0.1 (green) and 0.01 (red).

6. Conclusion

The Direct Numerical Simulations of a plane impinging jet were carried out for a dimensionless jet-to-surface spacing equal to 2. First, a laminar jet with a flat profile was simulated at $Re = 4000$, based on the jet velocity and width. Then, two cases using a fully-developed turbulent jet inlet were computed at $Re = 4000$ and $Re = 5700$.

The two cases at $Re = 4000$ allows to highlight the impact of the jet turbulence on the wall stresses and heat fluxes in the stagnation region. The laminar inlet case exhibits a secondary maximum in the Nusselt number profile at $Pr = 1$ where the impinged wall boundary layer transitions to turbulence. This secondary maximum is not present in the turbulent inlet case because the heat transfer in the region between the stagnation point and the transition region is increased by elongated streamwise vortices located near the bottom wall. The heat flux is similar in both cases just after the secondary maximum location. The wall shear stress is also increased by the mixing induced by those structures which originate from vortical structures of the jet being stretched in the stagnation region.

At low Prandtl, no secondary maximum is observed in the Nu profiles, even in the laminar inlet case, because the molecular diffusivity dominates the turbulent one. Therefore, the wall heat flux is less sensitive to the increase of the turbulent diffusivity related to the transition. Yet, a small increase of the Nu number is observed in the turbulent case compared to the laminar one.

The modification of the stagnation Nusselt number behavior at low Pr was shown by the different simulations. The laminar $Pr = 1$ and 0.1 cases are in good agreement with the relation proposed by Shadlesky [30], whereas the $Pr = 0.01$ case departs from this relation. It was shown for the turbulent cases that the stagnation Nusselt tends to only depend on the Peclet number, as typically observed at low Prandtl, and a new fitted correlation is proposed for low Prandtl number cases.

The turbulent cases at $Re = 4000$ and $Re = 5700$ show the same trends and the major differences are found in the Nu and C_f profiles. The transition of the bottom wall boundary layers also takes place slightly further away from the stagnation point at the larger Re. Yet, the $Re = 5700$ case, which corresponds to $Re_\tau = 181$ for the inlet turbulent profile, is better suited for RANS model calibration than the $Re = 4000$ case, corresponding to $Re_\tau = 133$, which can be difficult to reproduce by several RANS models not very well adapted to low Reynolds flows. This has been indeed reported in [31, 32] where the authors assessed different RANS approaches for the $Re = 4000$ case: the Peclet number of this case was rather small to clearly evaluate the turbulent heat flux modeling of the different RANS approaches at low Prandtl number even though the authors demonstrated the apparent inadequacy of the models based on the Reynolds analogy.

ACKNOWLEDGMENTS

The work described in this paper has been funded by the Euratom research and training programme 2014-2018 under grant agreements No. 654935 (SESAME) . The present research benefited from computational resources made available on the Tier-1 supercomputer of the Fédération Wallonie-Bruxelles, infrastructure funded by the Walloon Region under the grant agreement No. 1117545. Computational resources have also been provided by the Consortium des Equipements de Calcul Intensif (CECI), funded by the Fonds de la Recherche Scientifique de Belgique (F.R.S.-FNRS) under Grant No. 2.5020.11 and by the Walloon Region.

References

[1] P. Le Coz, J. F. Sauvage, and J. P. Serpantie. Sodium-cooled fast reactors: the ASTRID plant project. In *ICAPP 2011*, 2011.

[2] H. A. Abderrahim, P. Baeten, D. De Bruyn, J. Heyse, P. Schuurmans, and J. Wagemans. Myrrha, a multipurpose hybrid research reactor for high-end applications. *Nucl. Phys. News*, 20.1, 2010.

[3] G. Grötzbach. Challenges in low-Prandtl number heat transfer simulation and modelling. *Nucl. Eng. Des.*, 264(0):41 – 55, 2013.

[4] S Manservisi and F Menghini. A CFD four parameter heat transfer turbulence model for engineering applications in heavy liquid metals. *Int. J. Heat Mass Tran.*, 69:312–326, 2014.

[5] A. Shams, F. Roelofs, E. Baglietto, S. Lardeau, and S. Kenjeres. Assessment and calibration of analgebraic turbulent heat flux model for low-prandtl fluids. *Int. J. Heat Mass Tran.*, 79:589 – 601, 2014. ISSN 0017-9310.

[6] F. Roelofs, A. Shams, I. Otic, M. Böttcher, M. Duponcheel, Y. Bartosiewicz, D. Lakehal, E. Baglietto, S. Lardeau, and X. Cheng. Status and perspective of turbulence heat transfer modelling for the industrial application of liquid metal flows. *Nucl. Eng. Des.*, 290:99–106, 2015.

[7] M. Duponcheel, L. Bricteux, M. Manconi, G. Winckelmans, and Y. Bartosiewicz. Assessment of RANS and improved near-wall modeling for forced convection at low prandtl numbers based on les up to $Re_\tau = 2000$. *Int. J. Heat Mass Tran.*, 75:470–482, 2014.

[8] I. Tiselj. DNS of turbulent channel flow at Re_τ=395, 590 and $Pr = 0.01$. In *The 14th International Topical Meeting on Nuclear Reactor Thermalhydraulics, NURETH-14, 2011*, 2011.

[9] O. Errico and E. Stalio. Direct numerical simulation of low-prandtl number turbulent convection above a wavy wall. *Nucl. Eng. Des.*, 290: 87–98, 2015.

[10] G. M. Carlomagno and A. Ianiro. Thermo-fluid-dynamics of submerged jets impinging at short nozzle-to-plate distance: A review. *Exp. therm. fluid sci.*, 58:15–35, 2014.

[11] R. J. Goldstein B. Han. Jet-impingement heat transfer in gas turbine systems. *Ann. N. Y. Acad. Sci.*, 934:147–161, 2001.

[12] K. Nishino, M. Samada, K. Kasuya, and K. Torii. Turbulence statistics in the stagnation region of an axisymmetric impinging jet flow. *Int. J. Heat Fluid Flow*, 17(3):193–201, 1996.

[13] S. Satake and T. Kunugi. Direct numerical simulation of an impinging jet into parallel disks. *Int. J. Numer. Method H.*, 8(7):768–780, 1998.

[14] M. Hadziabdic and K. Hanjalic. Vortical structures and heat transfer in a round impinging jet. *Journal of Fluid Mechanics*, 596:221–260, 2008.

[15] D. Violato, A. Ianiro, G. Cardone, and F. Scarano. Three-dimensional vortex dynamics and convective heat transfer in circular and chevron impinging jets. *Int. J. Heat Fluid Fl.*, 37:22–36, 2012.

[16] T. Dairay, V. Fortuné, E. Lamballais, and L. E. Brizzi. Direct numerical simulation of a turbulent jet impinging on a heated wall. *J. Fluid Mech.*, 764:362–394, 2015.

[17] C. He and Y. Liu. Large-eddy simulation of jet impingement heat transfer using a lobed nozzle. *Int. J. of Heat and Mass Tran.*, 125:828 – 844, 2018.

[18] J. Taghinia and M. D. M. Rahman. Large eddy simulation of round impinging jet with one-equation subgrid scale model. *Int. J. Heat and Mass Tran.*, 116:1250 – 1259, 2018.

[19] J. Sakakibara, K. Hishida, and M. Maeda. Vortex structure and heat transfer in the stagnation region of an impinging plane jet (simultaneous measurements of velocity and temperature fields by digital particle image velocimetry and laser-induced fluorescence). *Int. J. Heat Mass Tran.*, 40(13):3163–3176, 1997.

[20] J. Sakakibara, K. Hishida, and W. R. C. Phillips. On the vortical structure in a plane impinging jet. *J. Fluid Mech.*, 434:273–300, 2001.

[21] H. Hattori and Y. Nagano. Direct numerical simulation of turbulent heat transfer in plane impinging jet. *Int. J. Heat Fluid Flow*, 25(5): 749–758, 2004.

[22] J. E. Jaramillo, F. X. Trias, A. Gorobets, C. D. Pŕez-Segarra, and A. Oliva. DNS and RANS modelling of a turbulent plane impinging jet. *Int. J. Heat Mass Tran.*, 55(4):789–801, 2012.

[23] P. Aillaud, F. Duchaine, L.Y.M. Gicquel, and S. Didorally. Secondary peak in the nusselt number distribution of impinging jet flows: A phenomenological analysis. *Physics of Fluids*, 28(9), 2016.

[24] O. V. Vasilyev. High order finite difference schemes on non-uniform meshes with good conservation properties. *J. Comp. Phys.*, 157(2):746–761, 2000.

[25] J. Kim, P. Moin, and R. Moser. Turbulence statistics in fully developed channel flow at low reynolds number. *J. Fluid Mech.*, 177:133–166, 1987.

[26] R. Moser, J. Kim, and N. Mansour. Direct numerical simulation of turbulent channel flow up to $re_\tau = 590$. *Phys. Fluids*, 11(4):943–945, 1999.

[27] J. Jeong and F. Hussain. On the identification of a vortex. *J. Fluid Mech.*, 285:pp 69–94, 1995.

[28] F. Beaubert and S. Viazzo. Large eddy simulations of plane turbulent impinging jets at moderate reynolds numbers. *Int. J. Heat Fluid Flow*, 24(4):512 – 519, 2003. Selected Papers from the Fifth International Conference on Engineering Turbulence Modelling and Measurements.

[29] L. Bricteux, M. Duponcheel, I. De Visscher, and G. Winckelmans. LES investigation of the transport and decay of various-strengths wake vortices in ground effect and subjected to a turbulent crosswind. *Phys. Fluids*, 28(6), 2016.

[30] P. S. Shadlesky. Stagnation point heat transfer for jet impingement to a plane surface. *AIAA J.*, 21:1214–1215, 1983.

[31] A. De Santis, A. Villa Ortiz, A. Shams, and L. Koloszar. Modelling of a planar impinging jet at unity, moderate and low prandtl number: Assessment of advanced rans closures. *Annals of Nuclear Energy*, 129: 125 – 145, 2019.

[32] A. Shams and A. De Santis. Towards the accurate prediction of the turbulent flow and heat transfer in low-prandtl fluids. *Int. J. Heat Mass Tran.*, 130:290 – 303, 2019.